A detailed CFD analysis of flow patterns and single-phase velocity variations in spiral jet mills affected by caking phenomena

Carmine Sabia [a,b,*], *Giovanni Frigerio* [c], *Tommaso Casalini* [a], *Luca Cornolti* [a], *Luca Martinoli* [d], *Antonio Buffo* [b], *Daniele L. Marchisio* [b], *Maurizio C. Barbato* [a]

[a] *Department of Innovative Technologies, SUPSI, Polo universitario Lugano – Campus Est, Via la Santa 1, 6962 Lugano, Switzerland*
[b] *Department of Applied Science and Technology, Politecnico di Torino, Corso Duca degli Abruzzi 24, 10129 Torino, Italy*
[c] *Munit SA, Via Crocicchio Cortogna 6, 6900 Lugano, Switzerland*
[d] *Jetpharma SA, Via Sottobisio 42a/c, 6828 Balerna, Switzerland*

ABSTRACT

In this work we present a method to investigate the fluid-dynamics of a 3D, real-scale spiral jet mill when caking is occurring. CFD simulations are employed to deeply study the pressure and the velocity fields of the gas phase when the nozzles inlet pressure and the chamber diameter are varied to mimic the condition generated by the aggregates formation during the micronizaton process. The computational model is built replicating the experimental observation consisting in the fact that most of the crusts form on the outer wall of the chamber. Simulations underline that caking causes the deterioration of the classification capabilities of the system if the gas mass flow rate is kept constant at nozzles, allowing larger particles for escaping the system. It is shown that it is possible to mitigate this phenomenon by gradually reducing the gas mass-flow rate to keep constant the nozzles absolute pressure. This keeps unchanged the fluid spin ratio and the classification characteristics when caking is advancing.

1. Introduction

Spiral jet milling (SJM) is a widely used industrial process able to reduce in size solid particles without the usage of any mechanical or moving part. The application fields of this technology are different, ranging from the micronization of pigments or mineral materials to the production of APIs (Active Pharmaceutical Ingredients) for the pharmaceutical industry (Midoux et al.,1999).

The absence of mechanical components in relative motion avoids powders contamination and leads to the possibility of obtaining highly pure and very fine particles with a narrow particle size distribution (PSD). Pharmaceutical active substances are micronized to achieve selected sizes, to increase specific surface area which enhances their dissolution rate, to maximize drug bioavailability and to dry powders from solvents used during the crystallization process (Nakach et al., 2019). SJM is often added at the end of a separation process (such as crystallization or freeze-drying) to tailor and homogenize the PSD (Adali et al., 2020).

1.1. SJM working principle

Spiral jet mills are systems in which a high-speed gas flow is used to mill solid particles (see schematic in Fig. 1). Raw powders, with usu-

---

Nomenclature

Latin letters

a,b	Γ model parameters
A_t	Throat section [m^2]
c_p	Specific heat at constant pressure [J kg^{-1} K^{-1}]
C_μ	0.09, k–ε model coefficient
$C_1;C_{1,\varepsilon};C_2;C_{3,\varepsilon}$	model coefficients
d	Diameter [m]
d_{cut}	Cut size diameter [m]
D	Generic characteristic length [m]
e	Specific internal energy [J kg^{-1}]
h	Specific enthalpy [J kg^{-1}]
I	Unity tensor
k	Turbulent kinetic energy [m^2 s^{-2}]/specific heat ratio
L	Generic length [m]
m	Mass [kg]
$\dot{m}$	Mass flow-rate [kg s^{-1}]
p	Pressure [Pa]
P_b	Generation of turbulent kinetic energy due to buoyancy [kg m^{-1} s^{-3}]
P_K	Generation of turbulent kinetic energy due to mean velocity gradients [kg m^{-1} s^{-3}]
R	Gas constant [J kg^{-1} K^{-1}]
S	Deformation strain-rate tensor [s^{-1}]
t	Time [s]
t_p	Particle residence time [s]
T	Temperature [K]
v	Velocity vector [m s^{-1}]
v′	Velocity fluctuation vector [m s^{-1}]
v	Generic velocity component [m s^{-1}]
V	Volume [m^3]
x_i,x_j	Generic spatial coordinate [m]
y	Generic distance [m]
y+	Dimensionless wall distance
Y_M	Fluctuating dilatations term [kg m^{-1} s^{-3}]

Greek letters

α	Phase volume fraction
Γ	Blending function for velocity profile
ε	Turbulent kinetic energy dissipation rate [m^2 s^{-3}]
κ	Interparticle distance parameter
λ	Thermal conductivity [W m^{-1} K^{-1}]
λ_t	Turbulent thermal conductivity [W m^{-1} K^{-1}]
μ	Dynamic viscosity [Pa s]
μ_t	Turbulent molecular viscosity [Pa s]
ν	Kinematic viscosity [m^2 s^{-1}]
ρ	Mass density [kg m^{-3}]
σ	Turbulent Prandtl number
τ	Generic shear stress [Pa]

Subscript

abs	Absolute
crit	Critical
f	Fluid phase
g	Gas phase
k	Related to turbulent kinetic energy (k-equation)
lam	Laminar
n	Normalized
p	Particle
r	Radial

ref	Reference
t	Turbulent
ε	Related to turbulent kinetic energy dissipation rate (ε-equation)
θ	Tangential
0	Total quantities

Superscript

+	Related to the universal velocity profile (non dimensional distance and velocity)
T	Transpose

Non-dimensional groups

C_d	Drag coefficient
Ma	Mach number
Re_p	Particles Reynolds number
Re_y	Wall distance based turbulent Reynolds number
spin ratio	Spin ratio defined as the ratio between the radial "r" and tangential "θ" velocities
Stk	Stokes number

ally a mean particle/crystal size of 300–700 μm and a solid feed rate of 0.5–300 kg/h (Midoux et al., 1999), are entrained into a gas flow and injected into a cylindrical volume called "grinding chamber". In the latter, a high-speed dry air or nitrogen flow is guaranteed by a variable number of nozzles (from 4 to 12, depending on the mill dimensions). The position and the orientation of the nozzles (showed as angle β of Fig. 1a) are set to establish a vigorous swirled flow within the chamber. The gas gathers and moves the particles, accelerating and making them collide, striking one against the other and impacting the chamber walls. The impacts induce mechanical stresses on powder crystals, ending in fragmentation and breakage. The particles size reduction is usually controlled by changing the solid feed rate and the so-called grinding pressure, that is the pressure at the nozzles inlets. The latter is set depending on the particular powder milled and it usually ranges from 4 to 12 bar[g].

Spiral jet mills are built in two variants, according to the position of the powder feeder: the first has the feeder located tangentially to the milling chamber (Fig. 1b, top), the second has the feeder located with an inclination on the upper plate of the micronization chamber (Fig. 1b, bottom). To the best of the authors knowledge, there are no studies in the literature in which the effects of these different approaches has been investigated to assess which has the best comminution efficiency.

Solid particles classification (which governs the PSD in the outlet stream) is determined by the balance between drag and centrifugal forces experienced by the particles, and thus by the radial and tangential components of the velocity and particle size/mass. Centrifugal forces direct the larger particles to the outer periphery and away from the mill outlet, while drag forces dominate for finest particles that are carried out of the mill with the spent gas.

1.2. The caking problem and the "cut size" concept

A well-known problem affecting APIs micronization is the so-called caking, *i.e.*, the formation of large rigid aggregates that stick on the spiral jet mill walls reducing the useful volume of the grinding chamber. Caking modifies the flow field affecting the classification and the outlet PSD making difficult to match the target requirements set at the beginning of the grinding process. Crusts formation is strongly influenced by the micronized substance and the operating conditions. In some cases, the size of the aggregates increases in time and reaches a steady-state, as a result of the balance between the caking buildup and erosion forces exerted by the swirled flow field, in many others the apparatus gets chocked. As a consequence, the micronization activity must be regularly stopped for cleaning the jet mill, reducing the
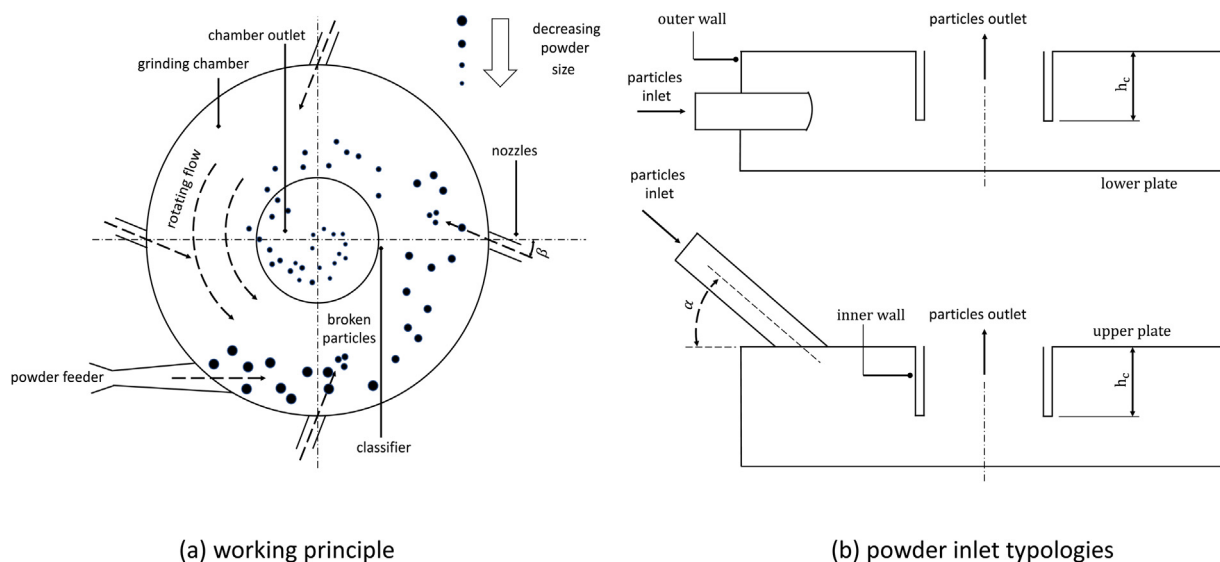
(a) working principle

(b) powder inlet typologies

Fig. 1 – Spiral jet milling working principle and system schematic.

(a) caking growth schematic
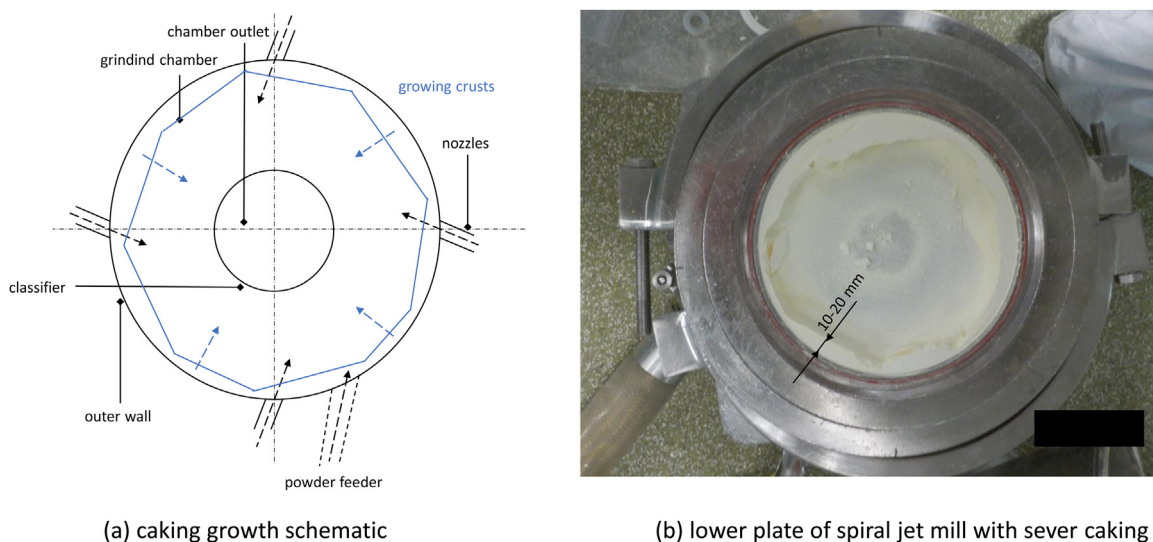
(b) lower plate of spiral jet mill with sever caking

Fig. 2 – Sever caking case and chamber diameter reduction, courtesy of Jetpharma SA.

effective production time. Moreover, crusts cannot be considered as a micronized product and reduce the process yield. This loss, along with the high cost of APIs (up to hundreds of thousands USD per kilogram), makes caking doubly detrimental from an economic point of view.

Because of its importance, caking was investigated in scientific literature. Van der Waals and electrostatic interactions as well as the presence of residual humidity have been identified as the main driving forces behind agglomeration (Zafar et al., 2017; Chen et al., 2018).

Carpin et al. (2017a,b) underlined that impurities and powder PSD have a strong influence on agglomeration. It was found that the higher is the particles specific area, the higher is the clustering tendency, meaning that fines have an important effect in generating crusts. It was also shown that the quantity of impurities, especially in humid environments, plays a major role in defining aggregates since they enhance the moisture sorption and water merges powders because of inter-particle bindings. The same findings were described by Listiohadi et al. (2008) while conducting investigations on storage experiments for polymorph lactose. The authors found relevant caking for all the lactose types at almost any relative humidity tested except for anhydrous α-lactose. Caking strength and stiffness were found to change significantly depending on the type of polymorph analyzed. Hardest cakes were obtained for anhydrous β- and spray-dried lactose that formed rigid structures apparently induced by partial fusion between crystals.

More in general, Hartmann and Palzer (2011) found that amorphous powders are prone to form clusters, discovering that the aggregates rigidity can be qualitatively linked to the sinter bridge diameter.

The caking of both crystal and amorphous powders was investigated in the work of Chen et al. (2019), who underlined that particles start aggregating mainly because of water (humidity) independently on the amount of crystal phase. Other important factors were reported to be the PSD and the particles shape.

Although studied in general, the caking mechanism for APIs was not extensively investigated and few examples are nowadays available in scientific literature.

Sowa et al. (2017) studied the possibility of improving the powder processability by working on the crystallization process of the granules. The authors found that the quantity of aggregates formed increased significantly with time, requiring the process stop to clean the apparatus. Brosh et al. (2014) attributed the sticky behavior of comminuted particles to Van der Walls forces and added their contribution to their Computational Fluid Dynamics – Discrete Element Method (CFD-DEM) simulation model availing of the work proposed by Kalman et al. (2009). The inclusion of the attractive interactions increased the agreement between simulation and experimental data. Among the factors affecting powder aggregation, Brunaugh and Smyth (2018) suggested that the amount of fines is one of the most important parameters promoting particles clustering and confirmed that electrostatics interaction due to Van der Waals forces favorite caking during spiral jet milling.

A representative example of severe caking is depicted in Fig. 2: aggregates with thickness ranging between 10 and 20 mm develop on the chamber periphery, while the crusts reach remarkably larger dimensions in the powder feeder proximity. The image clearly shows how particles agglomeration reduces the grinding chamber effective diameter and internal volume.

A mechanistic understanding of the influence of gas and solid flow on caking and vice versa is currently hindered by the challenging acquisition of experimental data; the effective application of sensors inside the chamber is difficult and can perturb the flow field, affecting the reliability of the measurement (Ma et al., 2001). On top of that, the involved physics are far from trivial, since they include fluid–solid interactions in a compressible, transonic (locally even supersonic) flow field. Furthermore, caking effects cannot easily measured even just correlating PSD values and agglomerates volume, because the latter is not known during the process. An evidence of this correlation can be inferred modeling the "cut size" concept. The latter is defined as the particle size for which the inertial forces on particles are balanced, i.e., a measure of which particle stays in and which particle goes out the jet mill. This approach requires to evaluate radial and tangential components of the gas flow velocity. MacDonald et al. (2016) developed a model for computing cut size as a function of geometrical and process parameters, gas thermodynamic properties and empirically-derived constants. However, many system-dependent parameters must be determined experimentally, potentially affecting the systematic and practical application of this model. It is important to notice that in a milling process affected by caking, these properties, and probably even the constants, would vary with time.

These arguments explain the absence of rigorous studies and the difficulties in predicting the outlet PSD (even without relevant caking phenomena). This scarcity of information leads to trial and error-based approaches, resulting in numerous, expensive and time-consuming tests (Bnà et al., 2020). The lack of a detailed picture of the involved phenomena and their synergic effects constitutes an obstacle to a more rational mill design and to the development of new effective solutions to avoid or dampen the attainment of caking.

1.3.   *CFD modelling of the spiral jet milling process*

In this scenario, the application of modeling tools like Computational Fluid Dynamics (CFD) constitutes an effective way to obtain those insights that could not be experimentally accessible, since they allow determining the flow field in every point of the grinding chamber, also accounting for the presence of a solid phase.

This approach has been widely used in the literature; Rodnianski et al. (2013) performed single-phase CFD simulation on a real-scale 3D spiral jet mill with twelve nozzles to obtain average flow fields and developed a classification equation based upon an analytic force model while the particles cut size was defined through experiments.

A recent work of Bnà et al. (2020) proposed a CFD-DEM approach with a soft gas–solid coupling in which the single-phase flow field inside a spiral jet mill was simulated via CFD and then used as frozen velocity field to transport particles with a Lagrangian approach. Collision frequency and energy for particles of different diameters were evaluated. The authors showed that it is possible to design a numerical method to simultaneously simulate discrete objects with two or three orders of magnitude difference in size in a reasonable time, by working with equivalent particles and keeping constant the product of particles diameter and density. Bnà and coworkers underlined the need of considering the phase mutual influence between the gas and the solid phases (4-way coupling), to keep track of the hold-up effects and their influence on particle-particle and particle-wall collisions.

Dogbe et al. (2017) used CFD-DEM approaches to numerically study the energy transfer between the carrier fluid and the particles, underlying how the collisions type is mainly constituted by particle-wall impacts for low particulate loading and by inter-particle interactions when the average volume fraction increases. The authors did not give any particular information on the primary phase flow characteristics within the jet mill, but states that particle-particle collisions are the predominant mechanism in size reduction events.

The absence of a direct experimental validation in these works corroborates the challenges related to a robust acquisition of experimental data; nevertheless, simulations provide a better understanding of the involved phenomena and constitute a first step towards the development of guidelines for a rational (and not trial-and-error-driven) mill design.

On the other hand, this approach has some limitations: CFD-DEM simulations are computationally intensive and currently do not allow simulating an industrial-scale process in a reasonable time. In addition, the inclusion of appropriate constitutive laws that describe particle breakage provides additional modeling and numerical challenges (Higashitani et al., 2020).

It was however proven in different works that precious information on the fate of the solid particles can be gained by simpler single-phase approaches (Boccardo et al., 2014, 2015, 2018, 2019; Crevacore et al., 2016, 2017; Icardi et al., 2014) in which the focus is on the continuous fluid (gaseous in this case) phase.

1.4.   *Work objective*

This constitutes the starting point for this work, which aims at investigating the impact of caking on the gas flow field (and thus on classification and outlet PSD) by means of single-phase CFD simulations. In more detail, caking is accounted for by progressively reducing the grinding chamber diameter to mimic particles clustering on peripheral walls.

2.   Spiral jet milling via Computational Fluid Dynamics

2.1.   *Fluid-dynamics model description*

The spiral jet mill fluid-dynamics model is calculated solving the Reynolds-Averaged Navier–Stokes (RANS) Equations discretized through the Finite Volume Method of ANSYS Fluent.

The single-phase flow field in an inertial reference frame with no gravity effects can be described through a set of partial differential equation of the form (Batchelor, 2000):

$$\frac{\partial \rho}{\partial t} + \nabla \cdot (\rho \mathbf{v}) = 0; \tag{1}$$

$$\frac{\partial (\rho \mathbf{v})}{\partial t} + \nabla \cdot (\rho \mathbf{v v}) = -\nabla p + \nabla \cdot (\tau). \tag{2}$$

The stress tensor τ is:

$$\tau = \mu[(\nabla \mathbf{v} + \nabla \mathbf{v}^T) - \frac{2}{3}(\nabla \cdot \mathbf{v})\mathbf{I}]; \tag{3}$$

where $\mathbf{v}$ is the 3D velocity vector, p is the pressure, μ is the molecular dynamic viscosity and $\mathbf{I}$ is the unity tensor.

The enthalpy ($h = e + \frac{p}{\rho} + \frac{\mathbf{v}^2}{2}$) equation is solved to consider gas compressibility effects, together with the ideal gas equation of state:

$$\frac{\partial \rho \left(h + \mathbf{v}^2/2\right)}{\partial t} + \nabla \cdot \left[\rho \mathbf{v} \cdot \left(h + \frac{\mathbf{v}^2}{2}\right)\right] = \frac{\partial p}{\partial t} + \nabla \cdot (\tau \cdot \mathbf{v})$$

$$+ \nabla \cdot \left[\frac{(\lambda + \lambda_t)}{c_p} \cdot \nabla h\right]; \tag{4}$$

$$\rho = \frac{p}{RT}; \tag{5}$$

where h is the specific enthalpy, ρ is density, λ is the molecular thermal conductivity, λ_t is the turbulent thermal conductivity, R is the gas constant and T is the temperature.

The turbulence nature of the flow is accounted for through the $k - \varepsilon$ realizable model (Shih et al., 1994):

$$\frac{\partial (\rho k)}{\partial t} + \nabla \cdot (\rho k \mathbf{v}) = \nabla \cdot \left[\left(\mu + \frac{\mu_t}{\sigma_k} \right) \nabla k \right] + P_k + P_b - \rho \varepsilon - Y_M; \quad (6)$$

$$\frac{\partial (\rho \varepsilon)}{\partial t} + \nabla \cdot (\rho \varepsilon \mathbf{v}) = \nabla \cdot \left[\left(\mu + \frac{\mu_t}{\sigma_\varepsilon} \right) \nabla \varepsilon \right] + \rho C_1 S \varepsilon - \rho C_2 \frac{\varepsilon^2}{k + \sqrt{\nu \varepsilon}}$$
$$+ C_{1\varepsilon} \frac{\varepsilon}{k} C_{3\varepsilon} P_b; \quad (7)$$

where k is the turbulent kinetic energy, ε is the turbulent kinetic energy dissipation rate, μ_t is the turbulent viscosity, σ_k and σ_ε are the turbulent Prandtl number for k and ε respectively. P_k represents the generation of turbulent kinetic energy due to mean velocity gradients while P_b is the generation of k due to buoyancy. Y_M is due to fluctuating dilatations in ε while C_1, C_2, $C_{1\varepsilon}$ and $C_{3\varepsilon}$ are model constants.

Reynolds stresses are computed through the turbulent viscosity concept and they are related to the fluid-flow mean velocity gradients availing of the Boussinesq approximation (Versteeg and Malalasekera, 2007), described by Eq. (8):

$$-\rho \overline{v_i' v_j'} = \mu_t \left(\frac{\partial v_i}{\partial x_j} + \frac{\partial v_j}{\partial x_i} \right) - \frac{2}{3} \left(\rho k \delta_{ij} \right). \quad (8)$$

Near-wall modeling is employed through the two-layer approach firstly proposed by Kader (1981); in which a continuous law obtained from the blending between the linear (laminar) and logarithmic (turbulent) functions is used to describe the whole velocity profile near the wall:

$$v^+ = e^{\Gamma} v_{lam}^+ + e^{1/\Gamma} v_t^+. \quad (9)$$

The wall-distance based turbulent Reynolds number defines the domain validity regions of the relations:

$$Re_y \equiv \frac{\rho y \sqrt{k}}{\mu}; \quad (10)$$

where y is the first cell-center distance while v^+ is the dimensionless velocity. Γ represents the blending function and has the form:

$$\Gamma = -\frac{a(y^+)^4}{1 + by^+}; \quad (11)$$

with y^+ equal to the dimensionless wall distance and a and b equal to model parameters.

2.2. Particles dynamics

Although the present study does not deal with the simulation of the particles motion, its comprehension and preliminary discussion is mandatory to understand which flow properties influence the solids trajectory and to correctly analyze single-phase simulations data.

In spiral jet mills, the particles position is determined by a force balance in which the competitive effects of radial and tangential components of velocity induce drag and centrifugal forces (see Fig. 3). A certain slip between the particles and the fluid velocities is established with a magnitude that is function of the object inertia (diameter and density), as showed by an early work of Konno and Saito (Rodnianski et al., 2013; Konno and Saito, 1969).

The quantity of solid particles that is instantaneously present within the grinding chamber is called mass hold-up and essentially defines the spatial-average particulate loading. The mass-hold up $m_{p,h}$ is related to powder feed-rate $\dot{m}_p$ and the average resident time t_p of particles (usually 10/15 s up to more than 100 s as showed by Mueller et al., 1996) inside the grinding chamber, reaching usual values of 5–30 g of powders (Bnà et al., 2020):

$$m_{p,h} = \dot{m}_p \cdot t_p. \quad (12)$$

The higher is the mass hold-up, the lower is the average inter-particles distance, with collisions that become more frequent when the solid feed-rate is augmented.

The ratio between solid and gas volume fraction κ gives the relative volume of particles with respect to the carrier phase:

$$\kappa = \frac{\alpha_p}{\alpha_g} = \frac{\alpha_p}{1 - \alpha_p}; \quad (13)$$

where α_p is the average solid phase volume fraction expressed as:

$$\alpha_p = \frac{\dot{V}_p}{\dot{V}_p + \dot{V}_g} = \frac{V_p}{V_p + V_g}. \quad (14)$$

The inter-particles (non-dimensional) distance L/d_p can be estimated availing of parameter κ, through the relation (Crowe et al., 2012):

$$\frac{L}{d_p} = \left(\frac{\pi}{6} \cdot \frac{1 + \kappa}{\kappa} \right)^{1/3}. \quad (15)$$

When the local α_p approaches 10^{-2} or larger values, the particles motion can influence the gas flow field and the inter-particles collisions may change significantly the particle trajectory.

Eq. (15) clearly shows that increasing the solid volume fraction results in an increase in the volume fraction ratio κ that causes a reduction on the inter-particle distance. Averaged quantities obtained from pure mass-flow analysis usually predict a dilute flow condition, with L/d_p ranging between 15 and 30.

The knowledge of the single-phase gas flow field is important to understand the particles driving force origin and the gas velocity maps in regions expected to have dilute concentrations. A certain quantity of the particles moving within the grinding chamber, indeed, aggregates on walls (Sowa et al., 2017) while the remaining part is more or less evenly distributed in the micronization volume. The latter can be used to compute the "average" volume fraction associated to particles that are not clustered and that are actually moving.

If the process takes place in a 200 mm spiral jet mill and 10 g of solid phase with a density of 1300 kg/m³ are assumed to move within the chamber, it is possible to compute an average particulate loading ranging between 5×10^{-3} and 10×10^{-3}, making reasonable the assumption of having a dilute flow condition (i.e., the solid particles do not influence the fluid flow).

The tendency of a particle to follow the fluid stream is strongly dependent on a non-dimensional group called Stokes
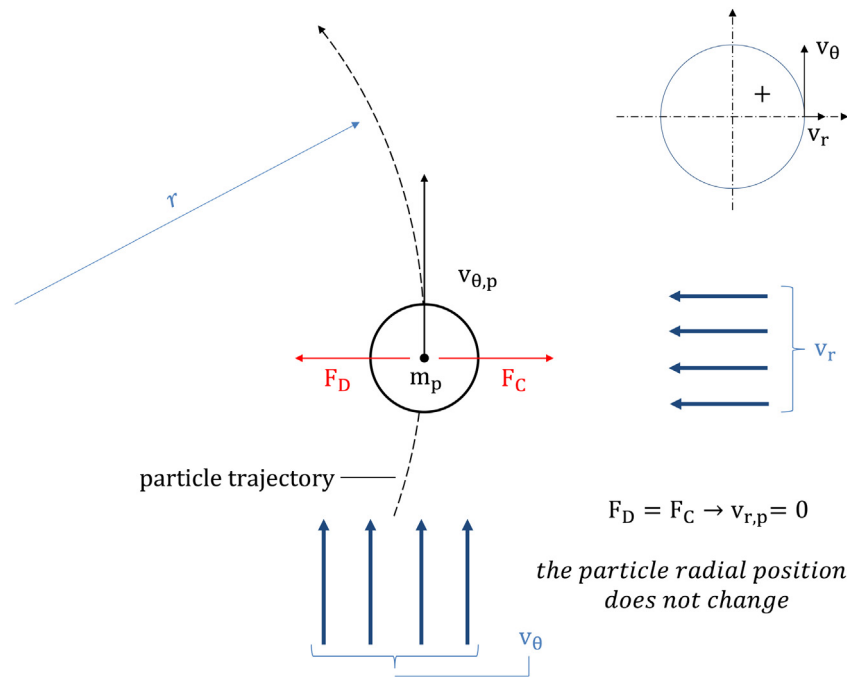
Fig. 3 – Schematic of the forces acting on a particle moving in a spiral jet mill chamber. Forces acting on a particle of mass m_p moving inside a spiral jet mill in the particular case of forces equal in value ($F_D = F_C$) are shown. The scheme is referred to the condition of particle radial velocity equal to zero, implying that the rotating object is moving over a circular trajectory of constant radius r. The blue arrows marked as v_θ (tangential velocity) and v_r (radial velocity) serve to depict the fluid flow velocity components which the particle is subjected to.

number that represents the ratio between the characteristic time of particles or droplets to the characteristic time of the fluid that moves them:

$$Stk = \frac{\rho_p \, d_p^2 \, v_0}{18 \, \mu_g \, D};$$

(16)

where ρ_p is the particle density, d_p is the particle diameter, v_0 is the fluid velocity far away from the particle, μ_g is the dynamic viscosity of the fluid surrounding the particle and D is a meaningful characteristic length that for spiral jet milling is usually the grinding chamber radius or diameter (Zhang et al., 2006). For Stk $\ll$ 1 the particles inertia is negligible if compared to body forces exerted by the fluid and they strictly follow the primary phase streamlines. If Stk approaches or exceeds the unity (Stk $\approx$ 1 or Stk > 1), then particles can detach from the carrier fluid. Bnà reports a four order of magnitude Stk number variation from 10^{-3} (d_p = 1 μm, particles following the gas flow) to 10^1 (d_p = 100 μm, particles moving with their own inertia), indicating that its range within the spiral jet mill can be wide and the particles motion typology in the chamber can vary a lot from side to side.

In order to understand which flow properties influence the particles classification, that is the conditions for which particles can leave the grinding chamber because their orbits becomes smaller than the classifier radius, it is useful to derive a simplified relation able to define the cut-size threshold. Assuming that particles are so small to be moved by the gas without having any relative velocity with respect to the latter (Stk $\ll$ 1) and that the solid volume fraction is small enough to have infrequent particle–particle collisions (dilute

flow, L/d_p > 20), an analytical expression can be derived as follow (Bnà et al., 2020):

$$d_{cut} = \frac{3}{8} d_p C_d \frac{\rho_f}{\rho_p} \left(\frac{v_r}{v_\theta} \right)^2;$$

(17)

where d_p is the particle diameter, C_d is the drag coefficient, ρ_f is the fluid (gas) density and ρ_p is the particle density. Density and velocities vary non-negligibly near nozzles due to the sudden gas expansion and achieve their maximum in the region near nozzles themselves, just inside the chamber.

Eq. (17) also shows that the ratio between the radial (v_r) and the tangential (v_θ) fluid velocity components plays a major role in defining the classification capabilities of the system. For this reason, it is convenient to define a non-dimensional group, named spin ratio (as defined by Rodnianski et al., 2013), and to carefully study its variation within the chambers:

$$spin \, ratio = \frac{v_\theta}{v_r}.$$

(18)

2.3. Insights on particles fracture mechanics

Pharmaceutical particles can undergo three different breakage mechanisms consisting in simple breakage, fragmentation and chipping (Salman et al., 2004), usually exhibiting a brittle or semi-brittle behavior. In general, their response to external forces is usually dependent on their diameter. Indeed, it has been shown that there is a particular size, called critical diameter (d_{crit}), for which the particles behavior changes: small particles tend to deform without breaking, while for larger particles with size bigger than d_{crit} the impact energy causes fragmentation usually without any plastic deformation (Rowe and Roberts, 1995).

The critical diameter strongly depends on the substance under consideration as well as mechanical properties such
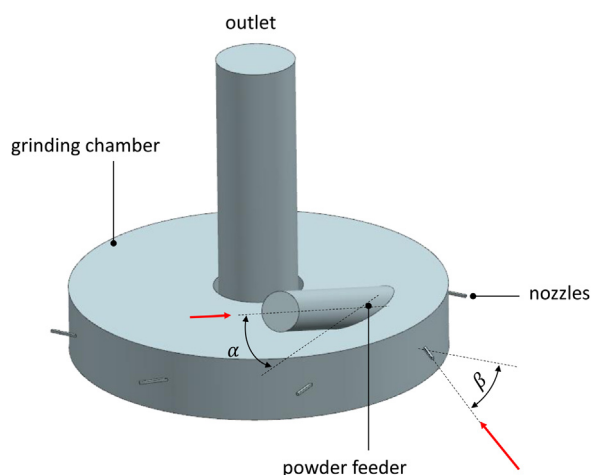
Fig. 4 – Simplified spiral jet mill computational domain.

as elastic modulus, indentation hardness and fracture toughness.

As example, Ibuprofen is reported to have $d_{crit} = 125 - 355\,\mu$m (Rowe and Roberts, 1995) while the Paracetamol one is about 7 μm (Shariare et al., 2012). If the collision energy is not enough to cause breakage, particles can be bounced back accumulating residual stresses that weaken bonds and make more likely the fragmentation at the subsequent impact. This mechanism is known as fatigue.

3.   Simulation model and numerical details

3.1.   Model description and boundary conditions

3.1.1.   Jet mill geometry, partitioning and caking mimic strategy
The simplified 3D computational domain consists in the fluid volume of a real-scale spiral jet mill that maintains all the most important features of the real geometry.

The geometry is composed by a cylindrical grinding chamber that hosts 8 constant square cross-section nozzles (Fig. 4). The powder feeder is bent by an angle α with respect to the chamber upper plate. The latter is connected to an outlet cylinder that allows for particles and process gas exiting. Geometry data cannot be shared because of confidentiality reasons; all dimensions are scaled with respect to a reference one.

Assuming that much of the crusts grow takes place on the outer wall of Fig. 1, caking is imitated by gradually reducing the chamber diameter to decrease the useful volume and simulate the particles clustering on walls to reproduce the condition depicted by Fig. 2. It can be observed from experiments that, in many micronization processes, the thickness of the aggregates sticking on the spiral jet mill walls does not exceed the 20% of the chamber diameter. This guided the computational domain generation and the chamber reduction strategy.

Fig. 5 shows that the geometry was designed to allow domain partitioning to build four different jet mills, named with f1 to f4. The four jet mills have a decreasing external diameter with a step equal to 7.5% passing from 100% (reference geometry, f1) to 77.5% (f4). Diameter f1 is taken as reference.

3.1.2.   Experimental data for boundary conditions
The fluid flow is composed by standard air whose main properties are reported in Table 5 of Appendix B.

The determination of proper boundary conditions for the jet mill nozzles is a difficult task. In fact, in spiral jet milling, properties can be usually measured where the gas flow is controlled, i.e. close to regulation valves and discharge points, and their evaluation is usually not possible inside the milling chamber.

Therefore, gauge pressure, temperature and volumetric flow rates were gathered during jet mill real operations and then manipulated to compute the gas mass-flow rate and to define local inlet boundary conditions. In particular, the sonic condition was exploited to apply an analytical expression at the nozzle inlets based upon the following assumptions:

 i 1-dimensional and steady-state flow, due to the fact that the gas characteristics change evolving along the nozzle direction, with no time-evolution effects;
 ii adiabatic flow, considering minor thermal exchange effects due to the rapid variations in flow properties;
 iii negligible friction, since the flow can be considered inviscid due to the high-velocity;
 iv ideal gas, since air at those pressure and temperature conditions behaves like and ideal gas.

In these assumptions, the mass flow rate can be evaluated from nozzles chocking conditions, i.e., by the following expression (Cengel and Cimbala, 2006):

$$\dot{m} = p_0 \cdot A_t \left[\frac{k}{R \cdot T_0} \left(\frac{2}{k+1} \right)^{\frac{k+1}{k-1}} \right]^{\frac{1}{2}}, \qquad (19)$$

that basically states that the mass-flow is controlled by the throat area of the nozzles A_t and the total upstream quantities T_0 and p_0. The gas characteristics also play a role, through the values k and R that are the heat capacity ratio and the gas constant, respectively. In this work, the carrier phase is air and no other gases were accounted for. The influence of different carrier phases on the process can be eventually found in the PhD thesis of Bartholomäus (2018).

The spiral jet mill analyzed in this study has eight grinding nozzles and one powder feeder that is served by another nozzle with a larger throat section. The solution of Eq. (19) gives the mass-flow rate passing through each grinding nozzle, and its multiplication by eight reports the total grinding gas mass per unit time. The total air consumption measured by experiments is then used to compute the air mass flow rate passing through the Venturi tube of the powder feed. The fluid at inlets is assumed to be at the stagnation temperature T_0. As reported by Table 1, the simulations of all four mill geometries are conducted for two different operating conditions:

- i: constant absolute pressure @ nozzles inlet while the chamber diameter is reduced by 7.5% (f1 = 100% to f4 = 77.5%)
- ii: constant gas mass flow rate @ nozzles inlet while the chamber diameter is reduced by 7.5% (f1 = 100% to f4 = 77.5%)

Case 01 in Table 1 is taken as reference case and its mass-flow rate and absolute pressure conditions, originally computed starting from experimental data, are used to define BCs for the other simulations, according to condition i or ii.

Condition ii is intended to simulate the usual operating regime experienced by a spiral jet mill with severe caking taking place, in which the gas usage does not vary during the process and its mass-flow rate is kept constant despite the
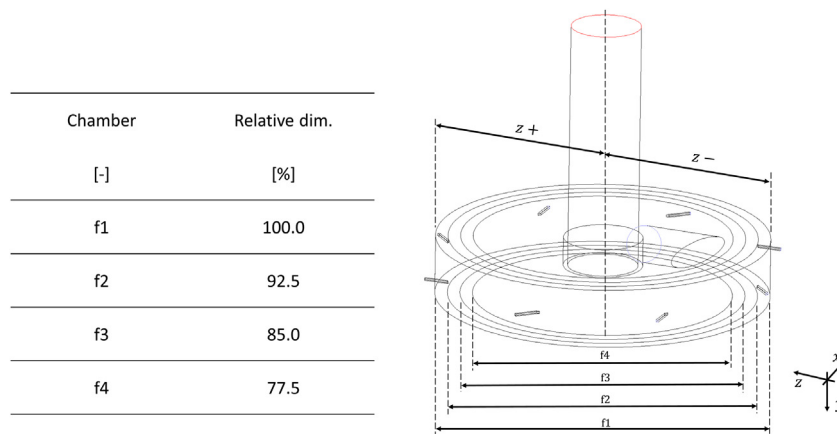
Chamber	Relative dim.
[-]	[%]
f1	100.0
f2	92.5
f3	85.0
f4	77.5

Fig. 5 – Detail of geometry splitting for chambers construction.

Table 1 – Simulations IDs and associated chamber dimensions/op. conditions.

Sim. name	Chamber	Op. condition	$mfr_{in}/mfr_{in,ref}$	$p_{abs,in}/p_{abs,in,ref}$	
01	f1	i/ii	1.00	1.00	**Chamber:**
02	f2	i	0.90	1.00	f1: chamber of radius 1 (largest)
03	f3	i	0.84	1.00	f2: chamber of radius 2
04	f4	i	0.78	1.00	f3: chamber of radius 3
05	f2	ii	1.00	1.11	f4: chamber of radius 4 (smallest)
06	f3	ii	1.00	1.19	**Op. condition:**
07	f4	ii	1.00	1.27	i absolute pressure @ nozzles = constant
					ii mass-flow rate @ nozzles = constant

crusts growth (increase in the absolute pressure by 9–11%). Condition i is used to test the effect that a reduction of the gas mass flow rate at inlets of 6–10% has on the fluid velocities when the diameter is reducing (caking is taking place), with the aim of maintaining constant the chamber absolute pressure and tune the velocities components.

Plots of Fig. 6 graphically represent the non-dimensional absolute pressure ratio (a) and non-dimensional inlet mass-flow ratio (b) between the actual value and the reference one as function of the mill chamber dimension and the operating condition.

3.2. Numerical solution

The CFD code used in this work is the commercial software Fluent by ANSYS (ANSYS, Inc, 2017).

The gas expansion through nozzles causes high velocities within them and the swirled streamlines inside the chamber causes the Mach Number (hereafter defined as Ma number) to overcome 0.3 in many regions. At these velocities the gas density becomes a strong function of temperature and pressure. In order to account for compressibility effects, air is assumed to behave like an ideal gas while the dynamic viscosity is kept constant to air standard value, since the extremely turbulent nature of the flow makes the eddy viscosity be predominant by orders of magnitude with respect to the molecular one.

In order to provide stability and robustness to the solution, the Pressure-Based Coupled Solver is used to solve Reynolds-Averaged Navier-Stokes equations (RANS). The pressure-correction and momentum equations are treated in a single step while the remaining relations (energy and turbulence model equations) are solved in a segregated manner.

As previously mentioned, turbulence was modeled through the two-equations $k - \varepsilon$ realizable model built upon the isentropic eddy viscosity approximation (Shih et al., 1994).

A two-layers law-at-the wall model is used to switch between the actual computation of the velocity profile till the first cell center ($y+ \approx 1$) and the usage of wall-functions ($y+ > 30$).

Gradients are discretized using the Green–Gauss Node-Based method (Barth and Jespersen, 2021) to obtain high-accuracy evaluations also for skewed cells. In order to well describe the pressure variation through nozzles and where the sudden expansions take place, pressure is interpolated at cell faces using momentum equation coefficients as described by Rhie and Chow (1983). Spatial discretization for momentum, energy and turbulent balances is obtained by the second-order upwind scheme, built upon the formalism proposed by Barth and Jespersen, ensuring drastic accuracy improvements with respect to first-order schemes even for mesh zones with abrupt changes in cell size and orientation.

Only steady-state solutions are investigated since the analysis is not aimed at studying the whole temporal dynamics of the system.

Pseudo-Transient Under-Relaxation (Kelley and Keyes, 1998) is used to implicitly under-relax transport equations and improve the convergence behavior by applying an artificial time-stepping.

The pseudo time-step is automatically computed by the solver according to the flow velocities inside the computational domain. A complete list of simulation numerical and physical settings, as well as the gas flow properties, is given in Tables 4 and 5 of Appendix B.

3.3. Analysis methodology

The analysis is conducted comparing the results, in terms of radial and tangential velocity components, over radial domain-crossing lines, as depicted by Fig. 7b. The sampling objects are built over the ix-plane and allows for collecting

(a) absolute pressure at nozzle inlet
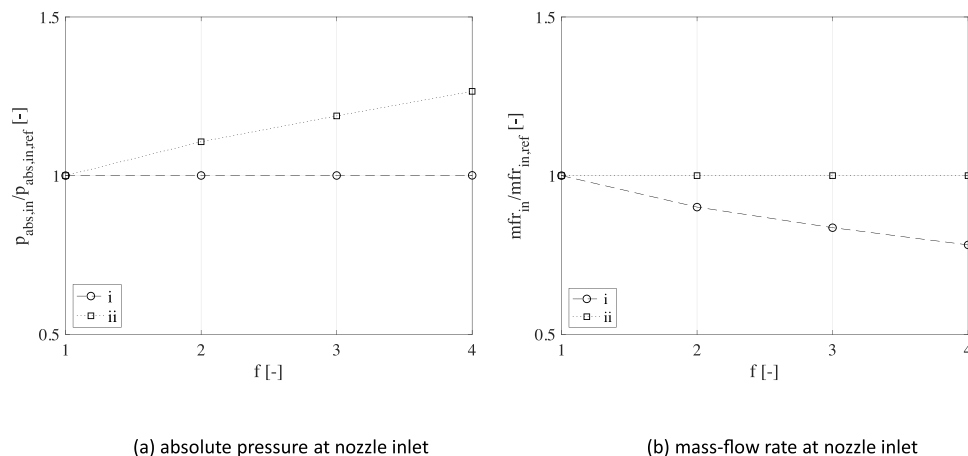(b) mass-flow rate at nozzle inlet

Fig. 6 – Non-dimensional absolute pressure ratio (a) and non-dimensional mass-flow rate ratio (b) between the actual and the reference value (01) of the property for the four chambers (f1–f4) and the two operating conditions (i,ii) analyzed.
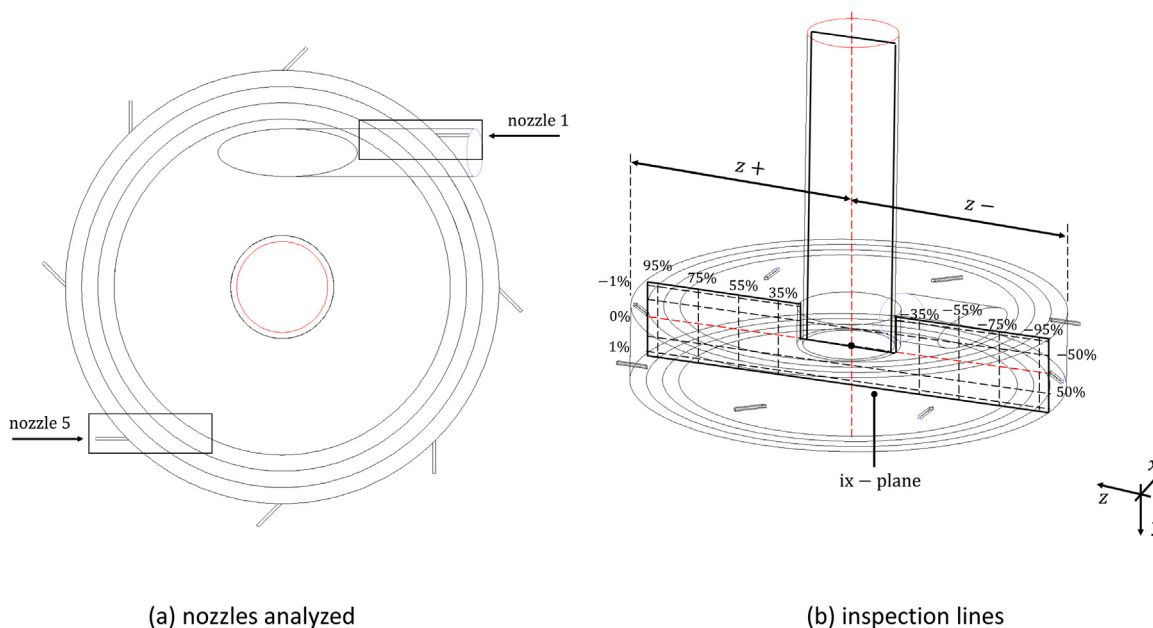

(a) nozzles analyzed
(b) inspection lines

Fig. 7 – Schematic of inspection lines for analysis results.

Table 2 – Mesh sensitivity analysis detail.			
Chamber	Nozzles cell-center wall distance [m]	y + max [–]	v max [m/s]
f1	8.3e-05	600	604.74
f1-finer	2.1e-05	220	608.87

data over five different lines in the radial direction and eight different lines along the chamber height. Relevant properties are also analyzed along the nozzles direction for the different chambers, in order to understand how the expansion of the carrier phase evolves when different geometries are used.

The analysis is completed by evaluating the dimensionless absolute pressure ratio and dimensionless density ratio defined as:

$$p_\mathrm{n} = \frac{p_{abs}}{p_{abs,ref}}, \tag{20}$$

$$\rho_\mathrm{n} = \frac{\rho}{\rho_{ref}}. \tag{21}$$

Data is scaled on purpose for confidentiality reasons. Pedix *ref* is used to identify average nozzles inlet properties of 01 case (f1, i/ii) used as reference.

3.4. Computational grids construction and mesh sensitivity analysis

The structured/paved computational grids were built in ANSYS Meshing following a multi-block approach. Elements were aligned with the flow direction in order to properly describe the rapid gradients variations in the flow properties.

The computational meshes have been evaluated controlling the mill maximum velocity with respect to the wall y^+ (Table 2) and analyzing the dimensionless absolute pressure ratio, the static temperature and the Ma number variation along nozzles (Fig. 8) in the proximity of nozzle 5.

Two mesh with a much different grid spacing have been studied. The coarse mesh has a maximum y^+ at nozzles walls of 600 while the fine one has a dimensionless wall distance always smaller than 220. The velocity maps obtained for the two grids, visible in the left part of Fig. 8, are completely comparable. The position and the shape of the supersonic plume
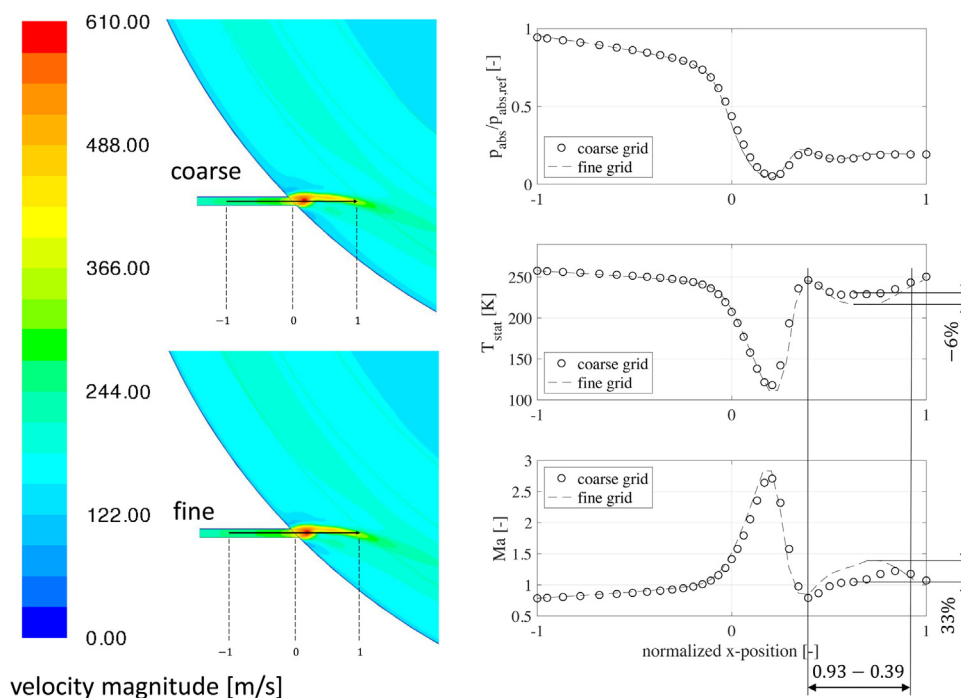
Fig. 8 – Contours of velocity magnitude (left) and properties variation along 0–1 segment (right) for Nozzle 5 in simulation 01 (i/ii), fine and coarse grids.

are exactly the same while the difference in the maximum velocity reached is less than 0.65%.

The dimensionless absolute pressure ratio, static temperature and Ma number evolution along nozzle 5 are depicted by Fig. 8. Data show that there is no appreciable variation between the coarse (dots) and the fine (dashed line) grid. The fine grid predicts a slightly larger expansion of the fluid flow, showing a reduction of 6% in static temperature and an increase of 33% of the Ma number.

The variation is limited to the last part of the supersonic plum (between coordinate 0.39 and 0.93 of the non-dimensional segment 0 → 1) and seems to affect a very localized region of the domain only.

Moreover, there is evidence (Bnà et al., 2020) that the pressure drop between inlets and outlet is well-predicted either with the fine or coarse mesh. Because of these results, together with the agreement between pressure predictions obtained with the coarse and the fine grid of Fig. 8, as well as the better convergence behavior obtained with the coarse one, the latter is then used as proper computational grid for the simulations and all the results presented hereafter are obtained with it. Details about the computational grids used can be found in Table 3 of Appendix A.

4. Results and discussion

Fig. 9 reports the dimensionless absolute pressure (a), static temperature (b), dimensionless density (c) and velocity magnitude (d) contour plots inside the grinding chamber f1. Images show an annular region of high velocity flow that moves around the chamber in proximity of nozzles. Pressure, density and temperature contours show that, apart from expansion regions downstream nozzles (detailed in the same figure), there is no abrupt properties variation within the chamber. The velocity maps (d) of Fig. 9 shows that the comminution chamber has an internal region in which the velocity is about 120–150 m s^{-1} and another one (previously called "annular

region") in which the velocity is in average between 150 and 250 m s^{-1}.

Contours of Fig. 9 also show that the outer zones have low pressure. Most of the temperature and density variations are localized into mill parts where larger expansions take place. The supersonic jets coming from nozzles appear to be deviated by the air flow already rotating inside the chamber. Plumes disappear washed out by the large volume flow rate passing through the jet mill. This behavior is also confirmed by previous observations made in earlier works (Bnà et al., 2020; MacDonald, 2007).

Fig. 10a depicts the streamlines generated by the flow coming from nozzles. As it can be seen the gas moves slowly from the outer part to the inner part of the grinding chamber, without an efficient mixing with gas entered by the powder feeder (Fig. 10b). Fig. 10b also shows that the air coming from the powder feeder remains segregated within the inner part of the chamber, located in the upper semi-half of the grinding volume. Due to this particular flow pattern drawn by the fluid coming from the powder feeder, it is clear that the classifier height (h_c of Fig. 1b) plays a major role in determining the cut size and therefore the classification capacities of the system. Its presence, indeed, constitutes a barrier and prevents the direct exit of fresh air that gathers the raw powders, allowing for keeping particles inside the comminution chamber to be grinded.

Fig. 11 shows the evolution of velocity magnitude contours and dimensionless absolute pressure, static temperature and Ma number along nozzle 5 of Fig. 7a for chambers f1, f2, f3 and f4 when constant pressure is imposed at inlets (operating condition i of Table 1). It is interesting to notice that the maximum expansion region is common to all simulations and it is located inside the chamber, while the supersonic condition is reached in the throat section of nozzles. Once chocking is established, the nozzles cross-section starts to enlarge because of the conjunction with the chamber and the flow experiences an enduring expansion similar to what hap-

(a) absolute pressure/reference absolute pressure [-]

(b) static temperature [K]

(c) density/reference density [-]
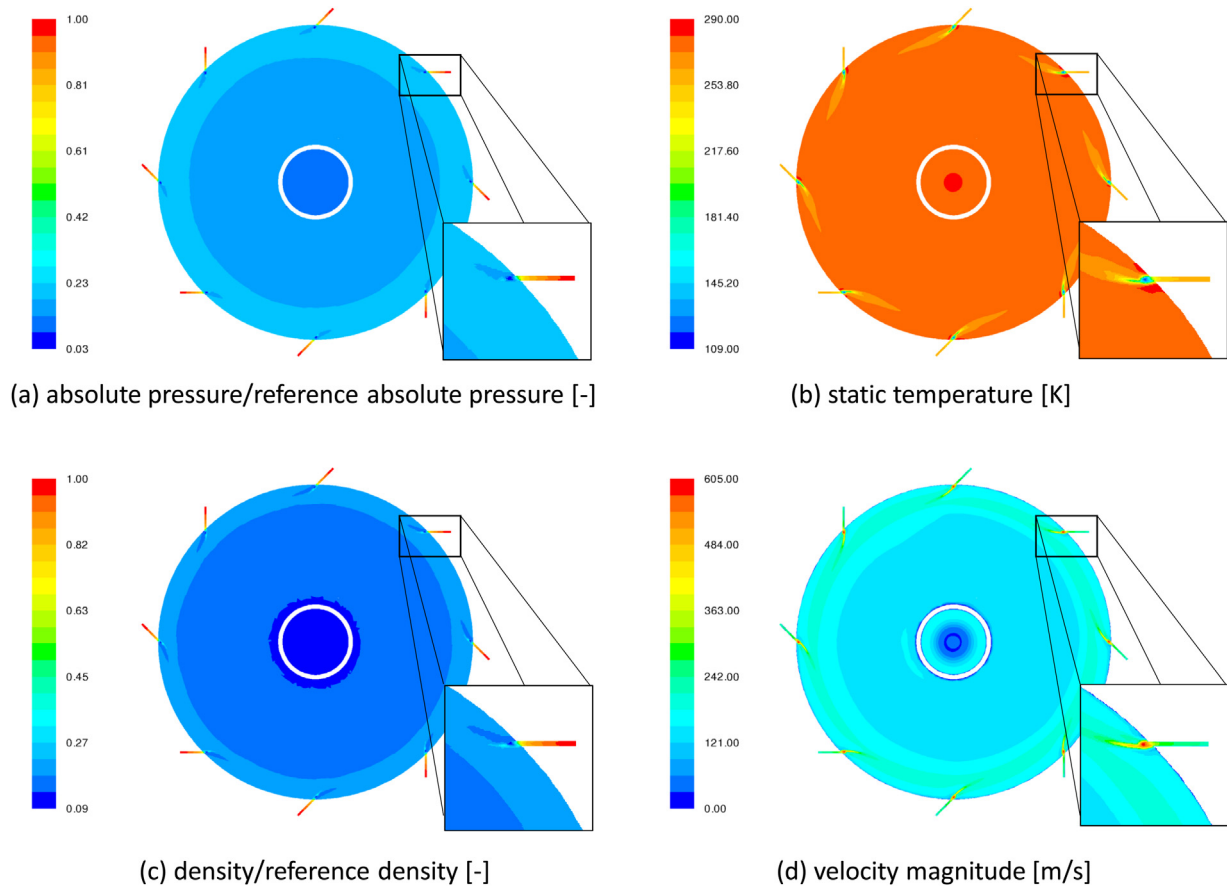
(d) velocity magnitude [m/s]

Fig. 9 – Flow property maps on the nozzles middle plane of simulation 01 (f1, i/ii). Pressure and density fields have been made dimensionless for confidentiality reasons by scaling the cell actual value for the reference taken at inlet nozzles. Detail of the nozzles maximum expansion region.
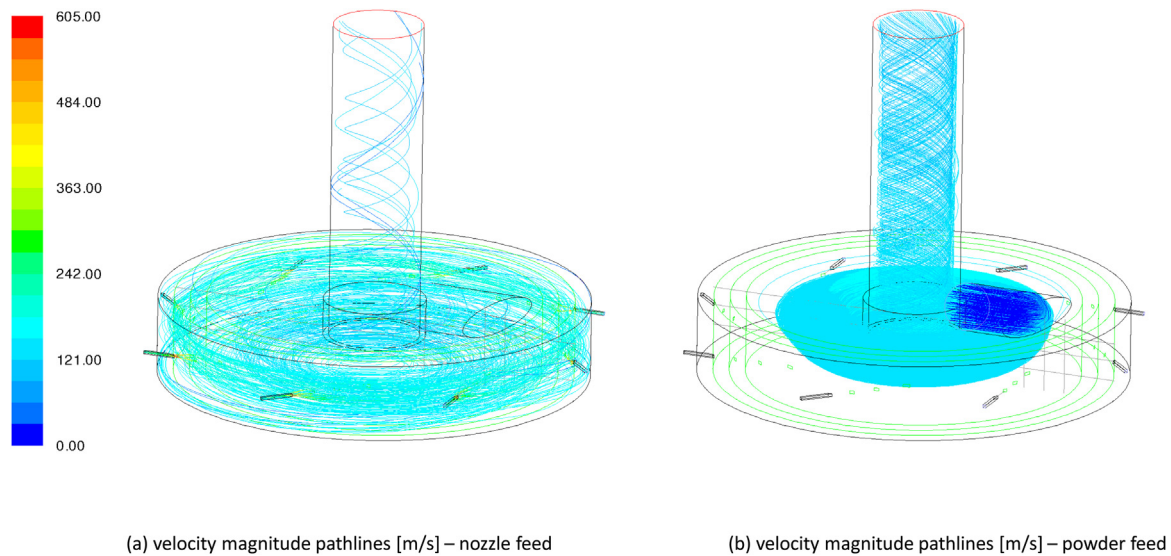

(a) velocity magnitude pathlines [m/s] – nozzle feed

(b) velocity magnitude pathlines [m/s] – powder feed

Fig. 10 – Flow pathlines colored by velocity magnitude of simulation 01 (f1, i/ii). The image represents the flow segregation experienced by the process fluid coming from nozzles (a) and the powder feed (b).

pens in De-Laval nozzles. The largest value for Ma number is found where the most abrupt variation of temperature and pressure is located and the position seems to be not influenced by the chamber dimension and, therefore, by the local flow condition. The maximum Ma value is, instead, a function of the mill diameter and the largest velocity is obtained for the reference chamber (f1), reaching a Ma peak approximately equal to 2.8.

The abrupt expansion takes the fluid temperature down to 108/110 K. The large gradients are limited to the supersonic plume and temperature rapidly raises to 250 K in the space segment 0 → 1. The absolute pressure also decreases till a value of 5–10% of the reference inlet pressure, well under the standard atmospheric pressure for a very limited portion of chamber. Results show that caking smooths oscillations and gradients after the maximum expansion but the conditions far from the latter are not influenced by the crusts presence.
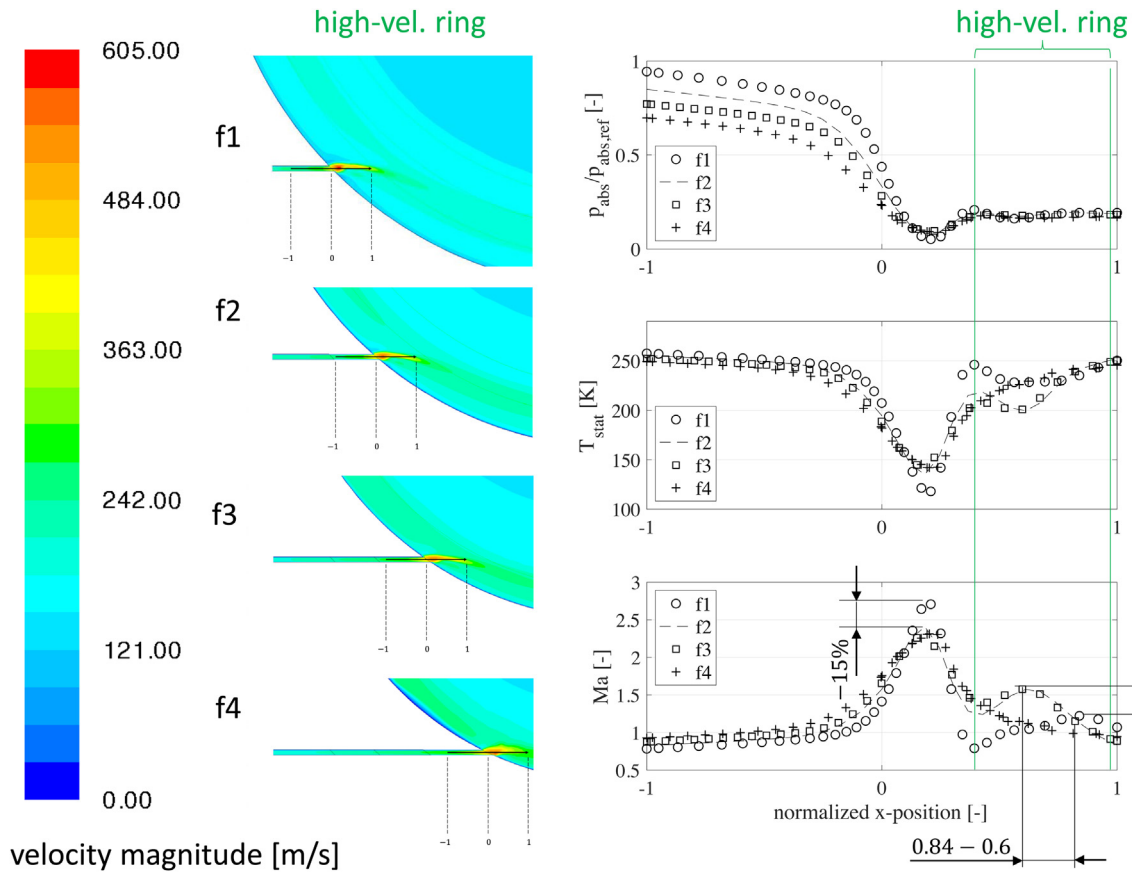
Fig. 11 – Contours of velocity magnitude (left) and properties variation along 0–1 segment (right) for Nozzle 5 in simulations 01–04 (f1-to f4, i).

The air already rotating inside the milling chamber tends to wash out the expansion, facilitating the recompression of the fluid at a similar value for all the mill dimensions. The toroidal region of high velocity fluid that rotates in the outer part of the chamber (green ring in the velocity maps of Fig. 11) is pushed towards the mill walls when the chamber radius is decreased, indicating that the rapid flow moving near nozzles is influenced by the spiral jet mill diameter and the gas motion tends to erode the crusts with higher intensity as the clustering becomes more efficient and aggregates occupy the chamber.

Non-dimensional absolute pressure decreases along segment $-1 \rightarrow 0$ as the mill chamber is made smaller while its value through the initial part of the comminution volume does not change significantly ($0 \rightarrow 1$). The opposite condition is found for temperatures and velocities that are affected by the chamber radius when the flow exiting the nozzles encounter the rotating fluid. A significant change in Ma number is found for chamber f1 with respect to the others, with a difference of 15% of the reference case. Although the reduction in the chamber diameter causes the smoothing of the peak expansion values for each property analyzed, chambers f2 and f3 show an increase of almost 30% of the local Ma number in the segment $0 \rightarrow 1$. The variation is very limited in space but points out how the caking phenomenon tends to smooth gradients and push high velocity zones towards the outer wall.

The radial and velocity components, as well as the inverse of the spin ratio, are shown in Fig. 12 (as function of the non-dimensional radial or z-coordinate) and Fig. 13 (as function of the non-dimensional height or y-coordinate). Cell-center data are gathered and plotted for the four mill chambers studied

and operating condition i, to simulate the effect that the reduction of the gas mass-flow rate has on the velocity components while caking is advancing.

Radial velocities, as depicted by Fig. 12, oscillate between −15 to 15 m/s over the whole domain except for very limited zones such the grinding chamber zone near the nozzles and the upper semi-half of the comminution volume that is affected by the presence of the powder feeder (Fig. 13). Nozzles cause a non-negligible peak in radial velocity, locally reaching a value of over −500 m/s, orders of magnitude larger than the average value in the rest of the chamber.

According to the scheme reported in Fig. 3, particles are often subjected to a null or a small positive radial velocity field and therefore they tend to move with their own direction. The nozzle jets push them towards the inner part of domain (negative radial velocities), especially if particles lie on the nozzles middle plane, where the radial and tangential components assume their highest value.

An equilibrium position can be reached only when particles move in a negative radial velocity field since inward components allow for obtaining a gas drag force that balances the centrifugal forces developed by the rotational motion of particles. Due to this reason, only a limited portion of the chamber is suitable for having a classification mechanism based upon aerodynamic forces.

Fig. 12 shows that in all chambers the radial velocities oscillate (b, f and j) changing sign, without the possibility of identifying a large region with a well-defined flow pattern. It is possible to recognize a small portion of negative continuous flow of gas only near the lower and the upper wall due to flow confinement towards plates (Fig. 14). Radial negative velocities
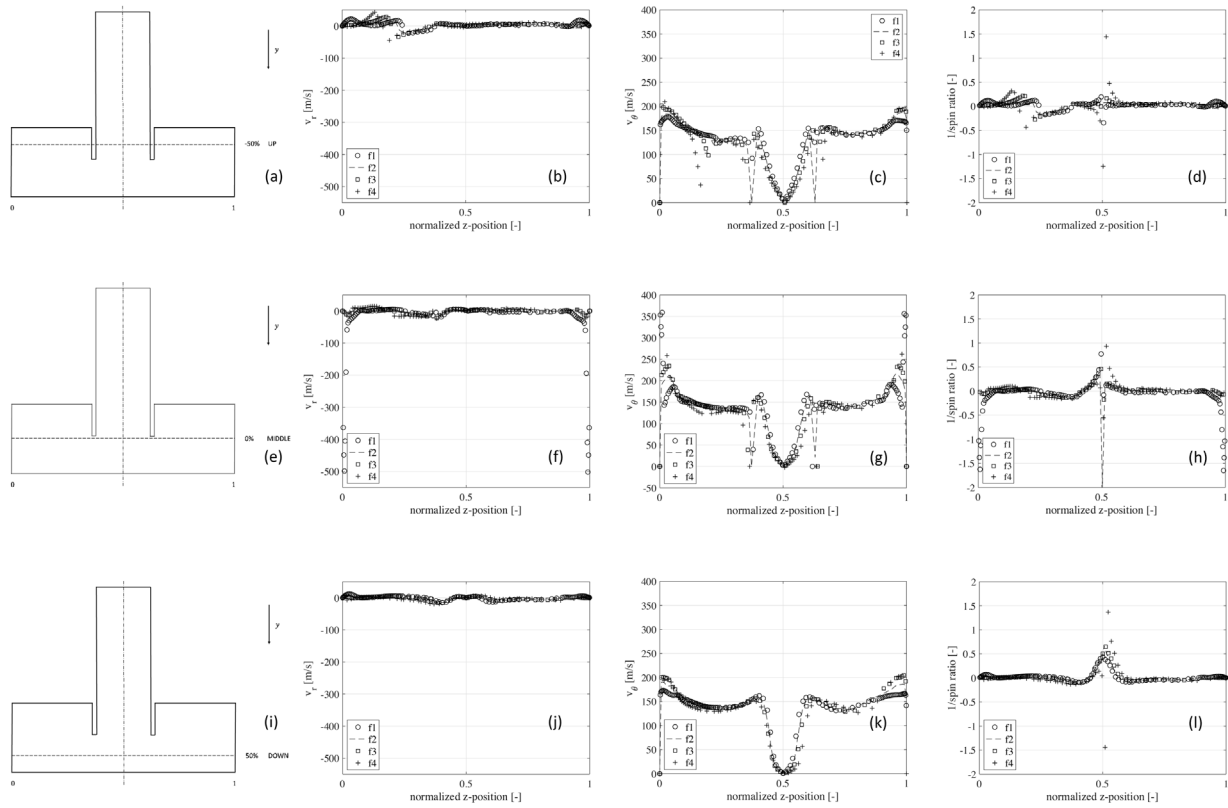
Fig. 12 – Radial velocity, tangential velocity and inverse of the spin ratio as function of normalized z-position along three different chambers height (f1 to f4, i).
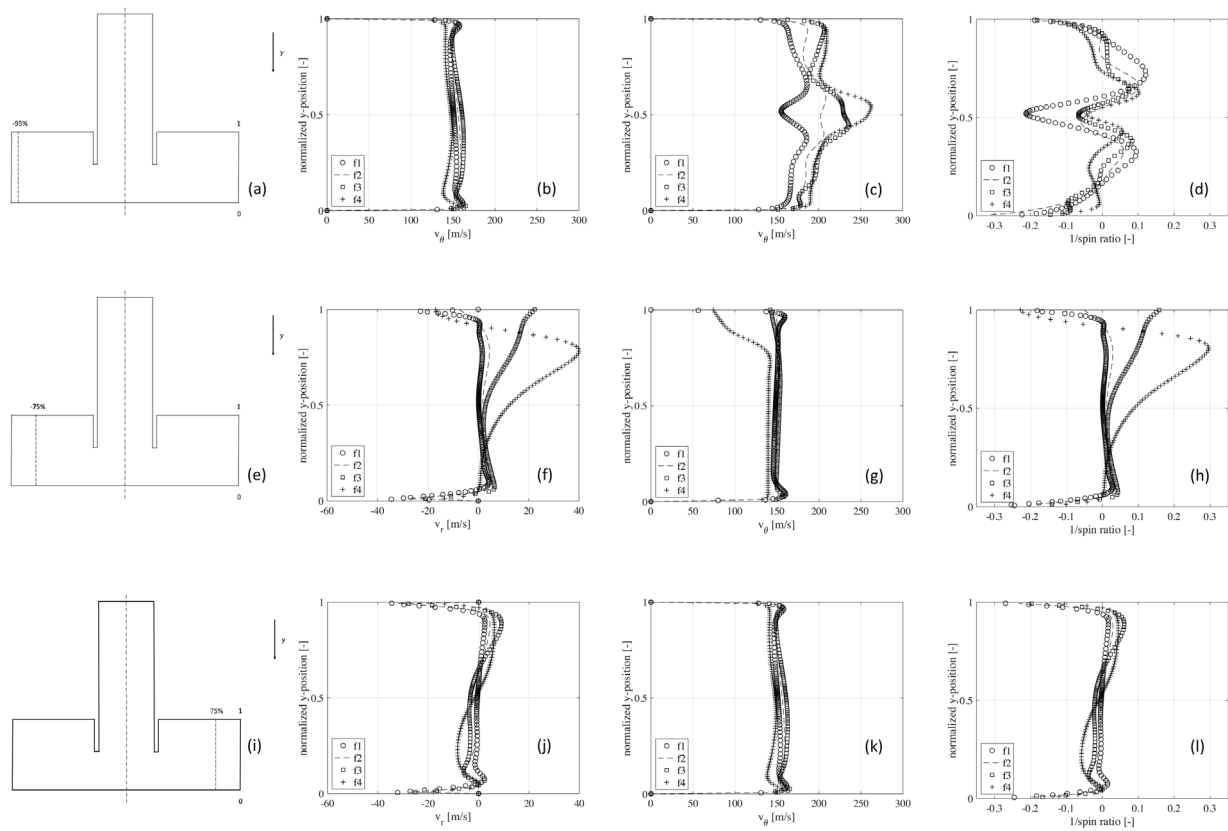

Fig. 13 – Radial velocity, tangential velocity and inverse of the spin ratio as function of normalized z-position along three different chambers radii (f1 to f4, i).

are also sampled at nozzles height, due to the inward gas flow coming from nozzles. The tangential velocity in the inner part of the chamber (0.09 < normalized z-position < 0.35 and 0.65 < normalized z-position < 0.91) show a uniform field except for the zones near the outer wall and the regions located in the center of the mill where tangential components go to zero

(a) f1 − i/ii, radial velocity [m/s]

(b) f1 − i/ii, negative radial velocity [m/s]
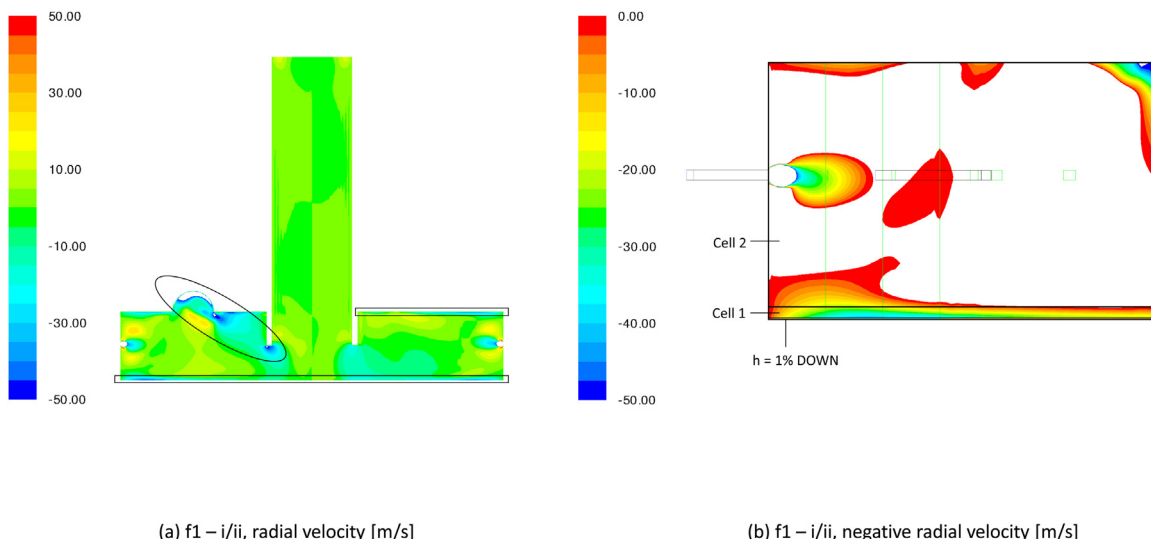
Fig. 14 – Scaled radial velocity maps on ix-plane (f1, i/ii). The two images are depicted in a "cut" scale to display only wanted velocities. White portions of figures contours show out-of-scale values (larger or smaller).
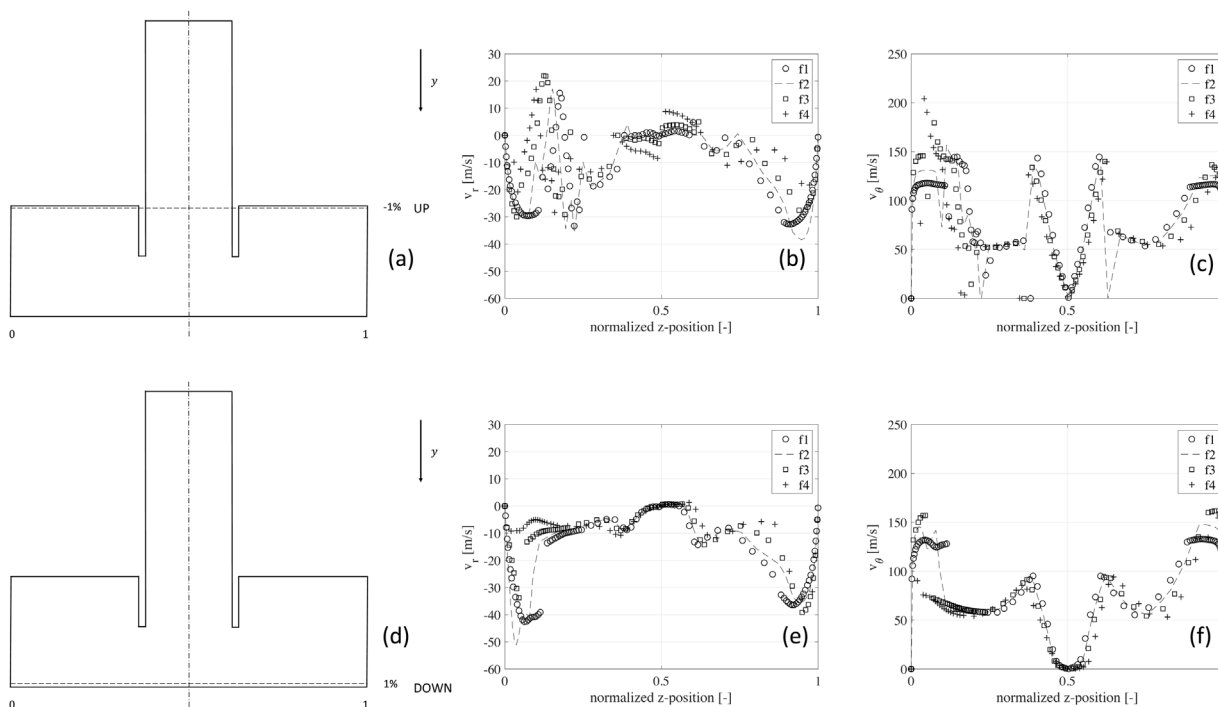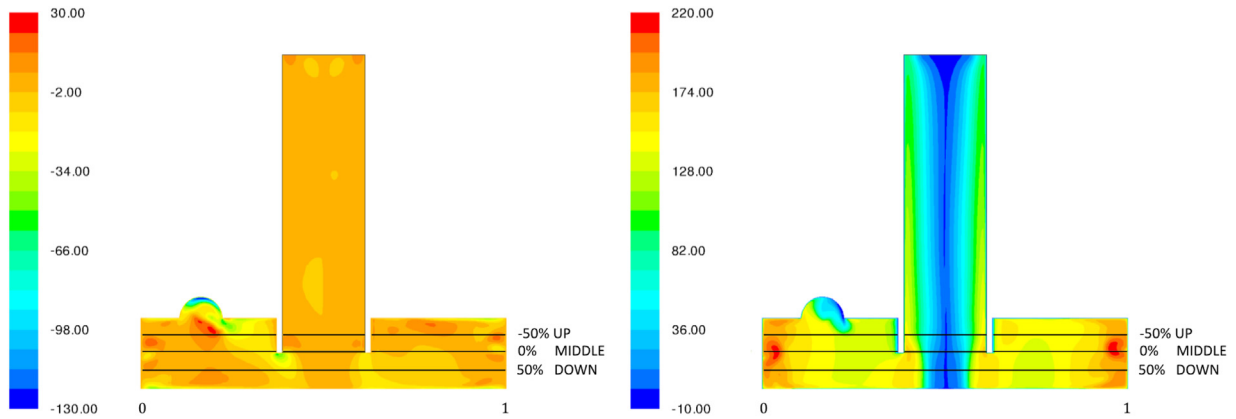

Fig. 15 – Radial and tangential velocity profiles as function of normalized z-position near the upper and lower mill walls (f1 to f4, i).

(plots c, g and k). The same observations made for radial velocity data can be done for the inverse of spin ratio (depicted in d, h, and l), with the remarkable difference of having large values at the center of the mill, induced by the null tangential velocity in that zone. These observations are also clearly stated by plots of Fig. 13, representing the radial velocity, tangential velocity and the inverse of spin ratio for the four chambers and operative condition i at three different lines evolving along the chambers height.

Tangential velocity at r = −75% (plot g of Fig. 13) gives similar values for every mill dimensions except for chamber f4, that shows a non-negligible decrease with respect to the others. The influence of the nozzles presence and the plume generated from the high-velocity flow coming from them is clearly shown by radial and tangential velocity peaks of plots at r = −95% (plots b and c). It is interesting to notice

that the radial velocity peaks show similar values as the chamber diameter is reduced while the tangential velocity component changes remarkably, increasing from f1 to f4. This phenomenon is confirmed by the inverse of the spin ratio, as showed by plot d of Fig. 13, that assumes the shape of radial velocity and shows values close to zero except for the near-nozzles regions, the portion of chamber near the powder feeder and the upper/bottom wall zones, where it increases and locally reaches $\frac{1}{\text{spin ratio}} < 0.2$, indicating that these zones are the most efficient in moving and sorting out particles (negative spin ratio with positive tangential velocity means negative radial components and therefore an inward flow). Plots h and l of Fig. 13 show that the original chamber f1 gives the most uniform velocities profile, while the others show an increasing inhomogeneity between the upper and the lower chamber semi-half. The spin ratio in the middle of the cham-
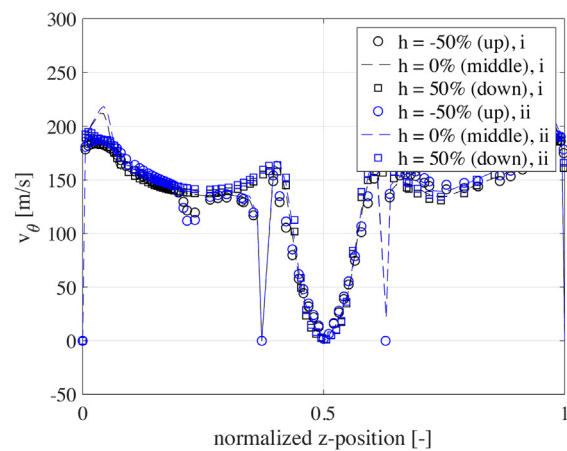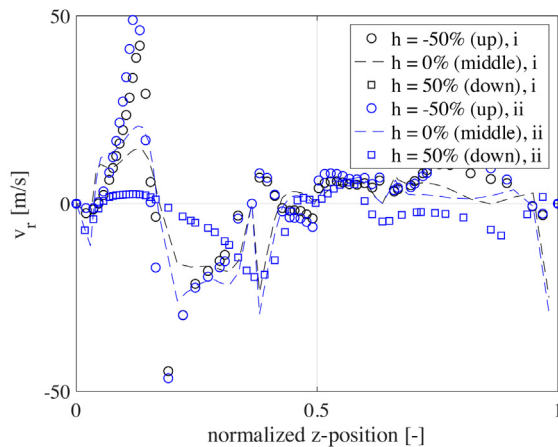
(a) f2 - i, radial velocity [m/s]
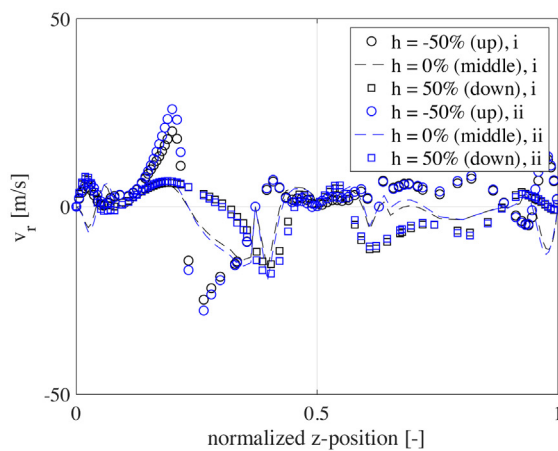
(b) f2 – i, tangential velocity [m/s]
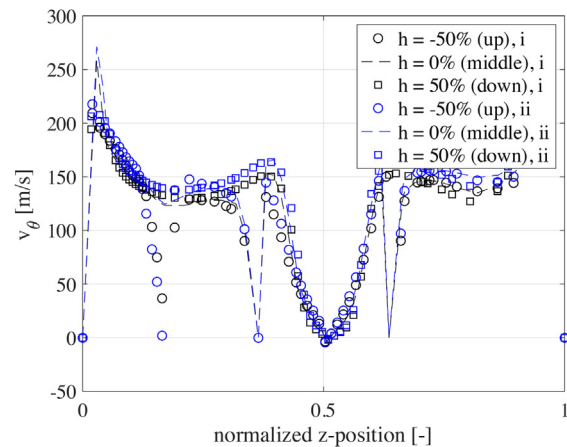

(c) f2, radial velocity [m/s]

(d) f2, tangential velocity [m/s]

(e) f4, radial velocity [m/s]
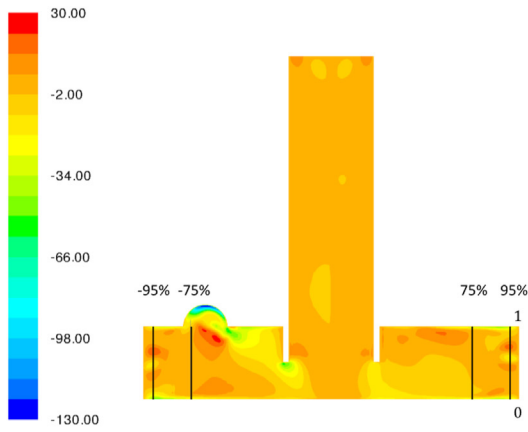

(f) f4, tangential velocity [m/s]

Fig. 16 – Radial and tangential velocity trends over three different chamber heights (f2/f4, i/ii).

bers does not change remarkably, indicating that the variation of the mill diameter has the major effect of changing the flow components repartition between the lower and the upper part of the grinding volume when the nozzles mass-flow is reduced.

Radial velocity contours plots shown in Fig. 14 underline that a large part of the comminution volume has positive radial velocity components. Positive velocities generate an outward flow that promotes collisions but not classification. Two thin regions of continuous inward radial velocity field can be identified near the upper and the lower plates, as depicted by the detailed plot of Fig. 14b. As previously reported, the powder feeder also generates a large inward flow that drives streamlines towards the system outlet.
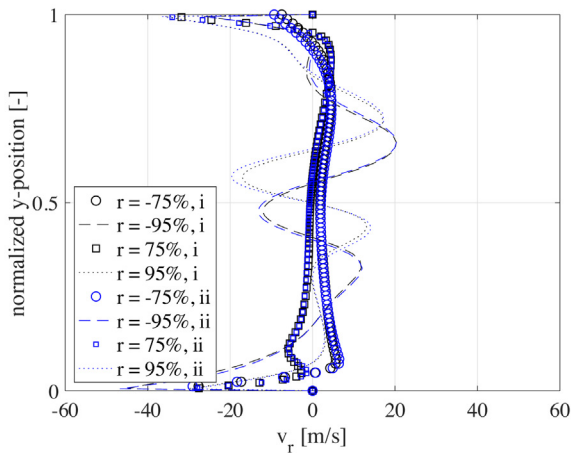
These observations show that the comminution volume of a spiral jet mill can be divided into three macro regions: a
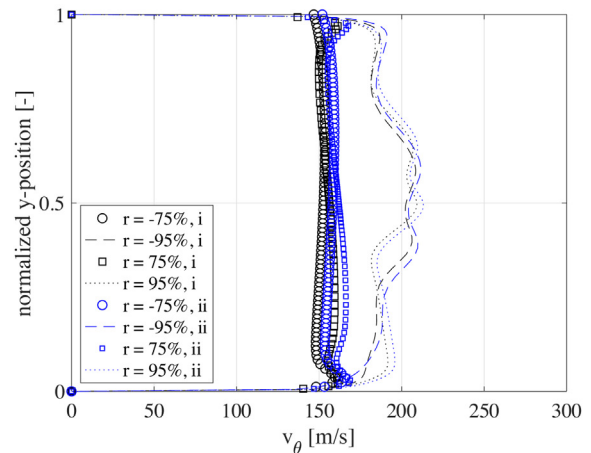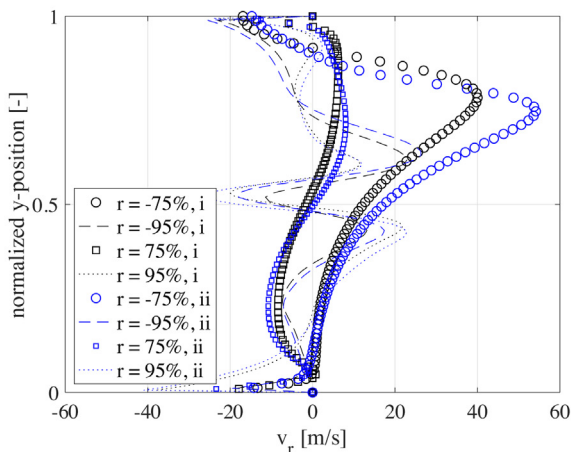
(a) f2 - i, radial velocity [m/s]
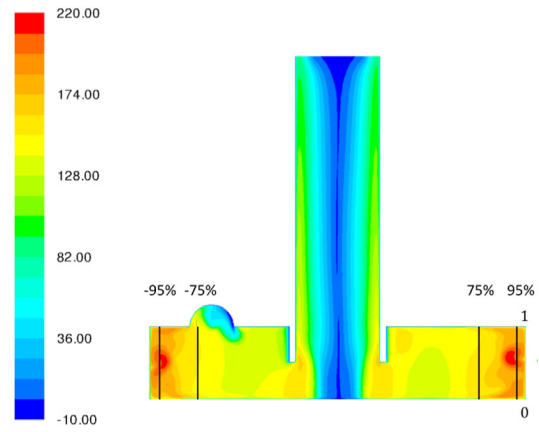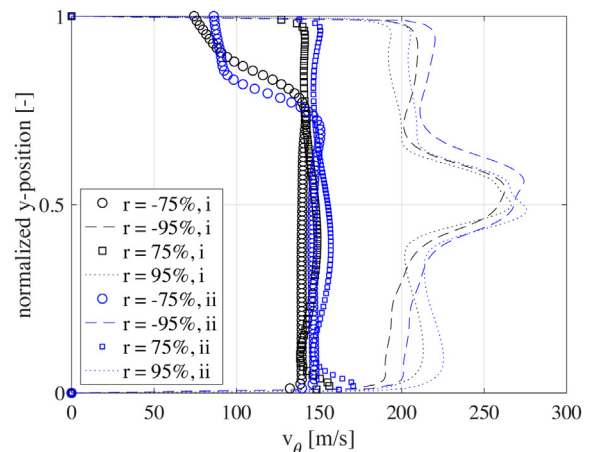

(b) f2 – i, tangential velocity [m/s]

(c) f2, radial velocity [m/s]

(d) f2, tangential velocity [m/s]

(e) f4, radial velocity [m/s]

(f) f4, tangential velocity [m/s]

Fig. 17 – Radial and tangential velocity trends over three different chamber radii (f2/f4, i/ii).

thin and localized zone near the lower wall (Cell 1 of Fig. 14b) with negative radial velocities, responsible of taking particles towards the outlet, a large zone located in the center of the chamber (Cell 2 of Fig. 14b) with positive radial velocity components that promotes collisions and another thin cell, similar to Cell 1, located near the upper wall that behaves like the latter.

Profiles located at 1% of the chamber semi-half height are shown by Fig. 15. A continuous region of negative radial velocities can be detected along the whole lower plate and along the right semi-half of the upper plate (plots b and e). The inward flow is much more vigorous going from the outer region towards the inlet, indicating that the carrier is more effective near the outer wall and in nozzles proximity. According

to the flow dynamics inside the chamber, gas velocity components in Cell 2 are responsible for the colliding particles motion while those of Cell 1 and 3 are responsible for driving particles towards the outlet.

For all the chambers and operating conditions tested, the particles transport towards the outlet takes place only in plates proximity while the particle-particle and particle-wall collisions are promoted in the central part of the comminution volume (cell 2 of Fig. 14). This functioning principle is proper of all spiral jet mills with tangential solid injection and with an upper discharge.

Tangential velocity profiles shown by plots c and f of Fig. 15 are similar in shape to those sampled at h = −50% and 50%, with the peculiarity of having a flatter and more uniform form near the lower plate than near the upper wall. This is reasonably induced by the powder feeder presence and by the tortuous way imposed by the classifier (h_c in Fig. 1b) to the gas flow. Plots b, f and j of Fig. 13 clarify that the high-velocity ring generated by the nozzles gas flow reaches also zones near the plates. The powder feeder strongly affects the left semi-half of the chambers, generating chaotic components that make the radial velocity change in sign and generate oscillations in tangential components (plots b and f of Fig. 12).

Fig. 16 depicts the radial (a) and tangential (b) velocity contours for chamber f2 as well as radial and tangential velocity data at different heights of chamber f2 (c and d respectively) and chamber f4 (e and f respectively).

Plots detail the velocity variation along the chambers radius, pointing out the difference that exists in radial velocity components when the chamber height is changed for the negative semi-plane, due to the powder feeder presence, also for sampling lines crossing the comminution volume in proximity of its median height. It is clear that there is a difference in sign between h = −50% and h = 50% in the positive z semi-half. The upper part of the chamber has only positive radial velocities while the bottom part presents negative values. This information, as depicted by the radial profiles of Fig. 15, plots c and e, confirms that the classification of particles can only take place in limited mill regions such as the lower part of the comminution volume. The three lines examined show that, in the left semi-plane, there is a negative radial velocity peak near the powder feeder region that is given by the local acceleration that the flow experience to move towards the outlet. This flow pattern is well recognizable for all the four chambers and both the operating conditions studied. The tangential velocity (plots d and f of Fig. 17) slightly increases near walls and drops down, as expected, in the center of the chamber.

As showed by Figs. 16 and 17, no remarkable difference is found in radial velocity profiles changing the operating condition from constant pressure (i) to constant mass-flow rate (ii) at nozzle inlets, especially for the sampling lines near the outer walls (r = −95% and r = −75%). A variation is observed only near the powder feeder that acts as a perturbation zone and locally modifies the radial velocity component showing a positive velocity peak (passing from i to ii) in chamber f4. The tangential velocity, instead, slightly increase in the whole domain, as showed by the difference between black and blue markers. It is interesting to notice that the modification of the gas mass-flow rate results in a variation of the tangential velocity (the higher is the mass-flow rate, the higher is the average tangential velocity), but it does not change remarkably the radial velocity component of the flow field. The variation of operating

condition i to ii increases the negative radial velocities in the plates proximity. To summarize, the increase of grinding pressure when the chamber diameter is reduced increases the gas tangential velocity in the central part of the chamber and the negative radial velocity component near plates. It enhances the flow patterns responsible of driving particles collisions but also the velocity field that causes particles classification.

This means that an effective strategy to control the classification capabilities of the spiral jet mills is to adjust the nozzles gas grinding pressure with the aim of tuning the spin ratio and customizing both the particles collision and the particles classification mechanisms.

5.   Conclusions

The internal gas dynamics of a spiral jet mill subject to caking phenomena was studied via single-phase CFD. A simple approach to mimic the grinding chamber diameter reduction due to solid particle agglomeration at walls was used. Four different caking conditions for the grinding chamber were explored and two different operating conditions, derived from relevant experimental data measured on a real-scale production plant, were reproduced. By focusing the analysis on radial and tangential velocity components as well as their dimensionless ratio (inverse of spin ratio), some general findings were achieved, able to explain the influence that the operating conditions, in terms of nozzles feeding pressure and chamber shrinkage (due to caking), have on the classification capacities of spiral jet mills with upper discharge and tangential solid feeding.

The analysis unveils that:

i   The gas flow is locally supersonic in regions downstream nozzles with large velocity, temperature and pressure gradients that arise from the sudden air expansion. The rest of the grinding chamber is transonic. The sonic choking in the nozzles throat sections is reached in every condition tested. It is possible to asses that caking does not affect the fluid flow in nozzles outlet proximity.

ii   The variation of the chamber diameter, for a given operating condition, has the main effect of modifying the homogeneity of the flow field. The velocity profiles are more uniform with the largest chamber while the others show an inhomogeneity between the upper and the lower semi-half of the comminution volume in terms of radial and tangential velocity profiles.

iii The reduction of the nozzle grinding total pressure along with the reduction of the chamber diameter (operating condition i) has the effect of keeping almost constant the spin ratio throughout the domain, with the exception of the zones located in the powder feeder proximity. This means that the nozzles mass-flow rate reduction while caking is advancing can control and avoid the classification of large particles due to aggregates formation.

iv   The increase of the nozzle total pressure along with the reduction of the chamber diameter (operative condition ii) causes the increasing of the tangential velocity components but not the radial one in the central part of the chamber. An increase of the radial velocities over the tangential ones is instead observed near plates and in the powder feeder proximity.

The analysis underlined how the inverse of spin ratio increases in the central part of the domain and remarkably

decreases near plates, becoming negative, promoting particles transport and taking larger objects towards the outlet.

This highlights that the largest part of the spiral jet mills grinding chamber is not suitable to classify particles since inward radial velocity components can be identified only near mill plates and in a limited region near the powder feeder.

Caking modifies the gas velocity field inside the micronization chamber (operative condition ii – constant mass flow rate at nozzles), by increasing the negative radial velocity component near plates and augmenting the classification capabilities of the system, taking out of specific the PSD of the final product.

In general, the spiral jet mills grinding chamber can be divided into three different cells, according to the radial velocity flow patterns: two thin zones located near plates (Cell 1) where the particles transport towards the outlet takes place and a large central zone (Cell 2) responsible of driving the solids phase collisions.

The reduction of the nozzles inlet pressure is identified as an interesting general control strategy to modulate the spin ratio and modify the classification capabilities of spiral jet mills by changing the radial velocity pattern near the plates and in the powder feeder proximity to counterbalance the effects induced by the crusts grow and keep the system working properly despite caking.

Given that particle segregation mainly takes place near the internal ring of the spiral jet mill and assuming that particles aggregate to form clusters on the outer part of the chamber when they reach large concentrations, the flow is considered as dilute and the analysis here described is limited to the gas fluid-dynamics. A fundamental step in the comprehension of the spiral jet mill process consists in the detailed simulation of the four-way fluid flow motion of gas and solid phases to properly describe the particles segregation, collisions and inertia. This analysis will be subject of a future communication.

6.   Declaration of competing interest

The authors declare that they have no known competing financial interests or personal relationships that could have appeared to influence the work reported in this paper.

CRediT authorship contribution statement

Carmine Sabia: Conceptualization, Methodology, Software, Validation, Formal analysis, Data curation, Writing - original draft, Visualization. **Giovanni Frigerio:** Validation, Resources, Writing - review & editing. **Tommaso Casalini:** Methodology, Validation, Writing - review & editing. **Luca Cornolti:** Methodology, Writing - review & editing. **Luca Martinoli:** Resources, Project administration, Funding acquisition. **Antonio Buffo:** Methodology, Writing - review & editing. **Daniele L. Marchisio:** Methodology, Writing - review & editing. **Maurizio C. Barbato:** Methodology, Formal analysis, Writing - review & editing, Project administration, Funding acquisition.

Acknowledgements

Appendix A. Details on the computational grids

Most important data regarding the computational grids used for calculations are listed in Table 3.

Mesh have been constructed availing of hexahedral elements and prisms whose morphology is represented in Fig. 18.

Table 3 – Computational grids data.				
Chamber	Elem. type	# [–]	Skewness max. [–]	AR max. [–]
f1	Hexa/prism	4'336'023	0.93	44.5
f1-finer	Hexa/prism	4'746'167	0.93	44.5
f2	Hexa/prism	3'393'423	0.93	44.5
f3	Hexa/prism	2'450'823	0.93	44.5
f4	Hexa/prism	1'508'223	0.93	44.5
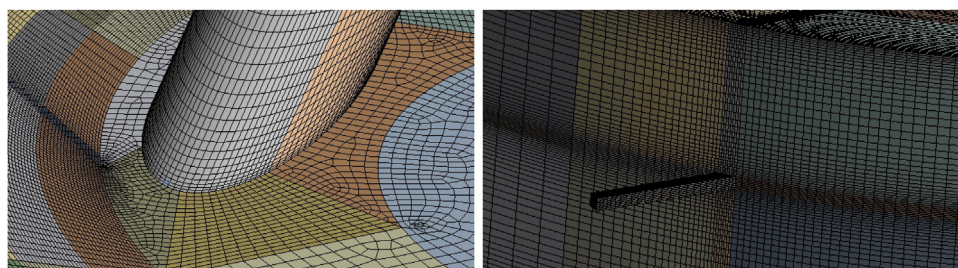
(a) powder inlet zone   (b) nozzles zone

Fig. 18 – Detail of the computational grids.

Appendix B. Numerical set-up, physical models and fluid properties

Table 4 – Numerical set-up.

Feature	Value/type/cond./eq.
Pressure-velocity coupling	Coupled solution
Velocity formulation	Absolute
Time formulation	Steady-state (pseudo transient)
Gravity	Off
Transport equations solved	Continuity
	x-, y-, z-momentum
	Energy
	Turb. kinetic energy
	Turb. energy dissipation rate
$k - \varepsilon$ model version	Realizable
Wall functions	Two-layer model (enhanced wall treat.)
Turb. model constants	$C_{1,\varepsilon} = 1.44$
	$C_2 = 1.9$
	$C_3 = 0$
	$\sigma_\mu = 1.0$
	$\sigma_\varepsilon = 1.2$
Residuals level	10^{-7}
	Energy $= 10^{-8}$
	Turbulence $= 10^{-3}$
Pseudo Transient Exp. Relax. Fac.	Pressure = 0.5
	Momentum = 0.4
	Density = 1.0
	Body force = 1.0
	Turb. kin. energy = 0.5
	Turb. diss. rate = 0.5
	Viscosity = 1.0
	Energy = 0.75

Table 5 – Fluid properties & physical models (air @ 288.15 K and 101,325 Pa).

Property	Symbol	Unit	Value/model
Density (formulation)	ρ_g	kg/m^3	Ideal gas law
Constant pressure specific heat	c_p	J/kg K	1006.43
Thermal conductivity	λ	W/m K	0.02
Dynamic viscosity	μ	Pa s	1.7894×10^{-5}
Specific heats ratio	k		1.4
Molecular weight	$\mathcal{M}$	g/mol	28.01

References

Adali, M.B., Barresi, A.A., Boccardo, G., Pisano, R., 2020. Spray freeze-drying as a solution to continuous manufacturing of pharmaceutical products in bulk. Processes 8 (6), art. no. 709.

ANSYS, Inc, 2017. ANSYS Fluent User's Guide, release 18.2.

Barth, T.J., Jespersen, D.C. The design and application of upwind schemes on unstructured meshes. 27th Aerospace Science Meeting.

Bartholomäus, L., 2018. Flow Conditions Inside Spiral Jet Mills and Impact on Grinding Performance. Universität Duisburg-Essen, Ph.D. Thesis.

Batchelor, G.K., 2000. An Introduction to Fluid Dynamics. Cambridge Univ, Online ISBN: 9780511800955.

Bnà, S., Ponzini, R., Cestari, R., Cavazzoni, C., Cottini, C., Benassi, A., 2020. Investigation of particle dynamics and classification mechanism in a spiral jet through computational fluid dynamics and discrete element methods. Powder Technol. 364, 746–773.

Boccardo, G., Marchisio, D.L., Sethi, R., 2014. Microscale simulation of particle deposition in porous media. J. Colloid Interface Sci. 417, 227–237.

Boccardo, G., Augier, F., Haroun, Y., Ferré, D., Marchisio, D.L., 2015. Validation of a novel open-source work-flow for the simulation of packed-bed reactors. Chem. Eng. J. 279, 809–820.

Boccardo, G., Crevacore, E., Sethi, R., Icardi, M., 2018. Robust upscaling of the effective particle deposition rate in porous media. J. Contam. Hydrol. 212, 3–13.

Boccardo, G., Sethi, R., Marchisio, D.L., 2019. Fine and ultrafine particle deposition in packed-bed catalytic reactors. Chem. Eng. Sci. 198, 290–304.

Brosh, T., Kalman, H., Levy, A., Peyron, I., Ricard, F., 2014. DEM-CFD simulation of particle comminution in jet-mill. Powder Technol. 257, 104–112.

Brunaugh, A., Smyth, H.D.C., 2018. Process optimization and particle engineering of micronized drug powders via milling. Drug Deliv. Transl. Res. 8, 1740–1750, http://dx.doi.org/10.1007/s13346-017-0444-x.

Carpin, M., Bertelsen, H., Dalberg, A., Roiland, C., Risbo, J., Schuck, P., Jeantet, R., 2017a. Impurities enhance caking in lactose powder. J. Food Eng. 198, 91–97.

Carpin, M., Bertelsen, H., Dalberg, A., Bech, J.K., Risbo, J., Schuck, P., Jeantet, R., 2017b. How does particle size influence caking in lactose powder? J. Food Eng. 209, 61–67.

Cengel, Y.A., Cimbala, M., 2006. Fluid Mechanics: Fundamentals and Application. The McGraw-Hill Companies, ISBN: 0-07-247236-247237.

Chen, M., Wu, S., Xu, S., Yu, B., Shilbayeh, M., Liu, Y., Zju, X., Wang, J., Gong, J., 2018. Caking of crystals, characterization, mechanism and prevention. Powder Technol. 337, 51–67.

Chen, M., Zhang, D., Dong, W., Luo, Z., Kang, C., Li, H., Wang, G., Gong, J., 2019. Amorphous and humidity caking: a review. Chin. J. Chem. Eng. 27, 1429–1438.

Crevacore, E., Tosco, T., Sethi, R., Boccardo, G., Marchisio, D.L., 2016. Recirculation zones induce non-Fickian transport in three-dimensional periodic porous media. Phys. Rev. E 94 (5), art. no. 053118.

Crevacore, E., Boccardo, G., Grillo, A., Marchisio, D.L., Sethi, R., 2017. Pore-scale simulations of particle transport for groundwater remediation: the effect of gravitational settling. Chem. Eng. Trans. 60, 193–198.

Crowe, C.T., Schwarzkopf, J.D., Sommerfeld, M., Tsuji, Y., 2012. Multiphase Flows With Droplets and Particles, second ed. CRC Press, Taylor & Francis Group, ISBN: 978-1-4398-4050-4054.

Dogbe, S., Ghadiri, M., Hassanpour, A., Hare, C., Wilson, D., Storey, R., Croley, I., 2017. Fluid-particle energy transfer in spiral jet milling. EPJ Web Conf., 140.

Hartmann, M., Palzer, S., 2011. Caking of amorphous powders – material aspects, modelling and applications. Powder Technol. 206, 12–121.

Higashitani, K., Makino, H., Matsusaka, S., 2020. Powder Technology Handbook, fourth edition. Taylor & Francis.

Icardi, M., Boccardo, G., Marchisio, D.L., Tosco, T., Sethi, R., 2014. Pore-scale simulation of fluid flow and solute dispersion in three-dimensional porous media. Phys. Rev. E Stat. Nonlin. Soft Matter Phys. 90 (1), art. no. 013032.

Kader, B.A., 1981. Temperature and concentrations profiles in fully turbulent boundary layers. Int. J. Heat Mass Transf. 24–9, 1541–1544.

Kalman, H., Rodnianski, V., Haim, M., 2009. A new method to implement comminution functions into DEM simulation of a size reduction system due to particle-wall collisions. Granul. Matter 11, 253–266, http://dx.doi.org/10.1007/s10035-009-0140-8.

Kelley, C.T., Keyes, D.E., 1998. Convergence analysis of pseudo-transient continuation. SIAM J. Num. Anal. 35-2, 508–523.

Konno, H., Saito, S., 1969. Pneumatic conveying of solids through straight pipes. J. Chem. Eng. Jpn. 2-2, 211–217.

Listiohadi, Y., Hourigan, J.A., Sleigh, R.W., Steele, R.J., 2008. Moisture sorption, compressibility, and caking of lactose polymorphs. Int. J. Pharm. 359, 123–134.

Ma, Z., van der Veen, H., Merkus, H.G., Scarlett, B., 2001. In-line particle size measurement for control of jet milling. Part. Part. Syst. Charact. 18, 99–106.

MacDonald, R., 2007. Optimization and Modelling of the Spiral Jet Mill. Newcastle University, Ph.D. Thesis.

MacDonald, R., Rowe, D., Martin, E., Gorringe, L., 2016. The spiral jet mill cut size equation. Powder Technol. 299, 26–40.

Midoux, N., Hosek, P., Pailleres, L., Authelin, J.R., 1999. Micronization of pharmaceutical substances in a spiral jet mill. Powder Technol. 104, 113–120.

Mueller, F., Polke, R., Schaedel, G., 1996. Spiral jet mills: hold up and scale up. Int. J. Miner. Process. 44–45, 315–326.

Nakach, M., Authelin, J.R., Corsini, C., Gianola, G., 2019. Jet milling industrialization of sticky active pharmaceutical ingredient using quality-by-design approach. Pharm. Dev. Technol. 24 (7), 849–863, http://dx.doi.org/10.1080/10837450.2019.1608449.

Rhie, C.M., Chow, W.L., 1983. Numerical study of the turbulent flow past an airfoil with trailing edge separation. AIAA J. 21-11, 1525–1532.

Rodnianski, V., Krakauer, N., Darwesh, K., Levy, A., Kalman, H., Peyron, I., Ricard, F., 2013. Aerodynamic classification in spiral jet mill. Powder Technol. 243, 110–119.

Rowe, R.C., Roberts, R.J., 1995. The mechanical properties of powders. Adv. Pharm. Sci. 7 (I-IV), 1–62.

Salman, A.D., Reynolds, G.K., Fu, J.S., Cheong, Y.S., Biggs, C.A., Adams, M.J., Gorham, D.A., Lukenics, J., Hounslow, M.J., 2004. Descriptive classification of the impact failure model of spherical particles. Powder Technol. 144, 19–30.

Shariare, M.H., Blagden, N., De Matas, M., Leusen, F.J.J., York, P., 2012. Influence of solvent on the morphology and subsequent comminution of ibuprofen crystals by air jet milling. J. Pharm. Sci. 101-3, 1108–1119.

Shih, T.H., Liou, W.W., Shabbir, A., Yang, Z., Zhou, J., 1994. A New k-ε Eddy Viscosity Model for High Reynolds Number Turbulent Flows-Model Development and Validation. NASA Technical Memorandum 106721, ICOMP-94–21; CMOTr-94-96.

Sowa, M., Klapwijk, A.R., Ostendorf, M., Beckmann, W., 2017. Particle engineering of an improved active pharmaceutical ingredient for improved micrometric properties. Chem. Eng. Technol. 40 (7), 1282–1292.

Versteeg, H.K., Malalasekera, W., 2007. An Introduction to Computational Fluid Dynamics. The Finite Volume Method, second ed. Pearsons – Prentice Hall, ISBN: 978-0-13-127498-3.

Zafar, U., Vivacqua, V., Calvert, G., Ghadiri, M., Cleaver, J.A.S., 2017. A review of powder caking. Powder Technol. 313, 389–401.

Zhang, L., Cheng, H., Zhang, C., Xu, Z., Ye, J., 2006. Deposit fraction of aerosol particles in a Human oral airway model on stable condition. Aerosol Air Qual. Res. 6–3, 259–267.